STUDY OF SUBSEA BLOWOUTS: REPORT ON A LARGE BUBBLE DYNAMICS STUDY

EE-121

91-05064/

STUDY OF SUBSEA BLOWOUTS: REPORT ON A LARGE BUBBLE DYNAMICS STUDY

by

J.D. Bugg and R.D. Rowe
Department of Mechanical Engineering
The University of Calgary
Calgary, Alberta

This report has not undergone detailed technical review by the Environmental Protection Directorate and the content does not necessarily reflect the views and policies of Environment Canada. Mention of trade names or commercial products does not constitute endorsement for use.

This unedited version is undergoing a limited distribution to transfer the information to people working in related studies. This distribution is not intended to signify publication and, if the report is referenced, the author should cite it as an unpublished report of the Directorate indicated below.

Any comments concerning its content should be directed to:

Environment Canada
Environmental Protection Directorate
River Road Environmental Technology Centre
Ottawa K1A 0H3

EE-121

AUGUST, 1990

Table of Contents

1.0 Summary 1

2.0 Test Facility Development 2
- 2.1 Flowmeters 2
- 2.2 Air Flow Symmetry 3
- 2.3 Run Matrix Revision 4

3.0 Flow Regime Mapping 5
- 3.1 Total Backflooding 5
- 3.2 Single Bubbles 5
- 3.3 Pairing 5
- 3.4 Larger Groups 6
- 3.5 Chains 6
- 3.6 No Backflooding 6
- 3.7 Flow Regime Map 6

4.0 High Speed Photography 8

5.0 Computational Results 11

6.0 Conclusions 12

7.0 References 13

APPENDIX A: Air Flow Symmetry Data 14

APPENDIX B: Paper submitted to The International Journal for Numerical Methods in Fluids 19

1.0 Summary

This report is a summary of work done at the University of Calgary, during the year April 1989 - March 1990, on the dynamics of bubbles formed at the exit of large submerged pipes. The work is intended to contribute to the fundamental knowledge of large bubble dynamics necessary to better understand and predict the behaviour of an undersea oilwell blowout very near the wellhead. Both an experimental and computational approach to the problem are being considered and progress to date in both areas will be summarised.

Last year's interim report (Bugg and Rowe [1989(a)]) discussed the commissioning of the large bubble dynamics test facility and presented some preliminary experimental results obtained by video and still photography. Based on the preliminary observations, it discussed some of the dominant phenomena that appeared to govern large bubble behaviour.

During this reporting period, some of the deficiencies identified in the commissioning of the test facility have been addressed and corrected. An additional critical venturi meter was machined to provide a wider range of flowrates. An updated form of the calibration curve for all flowmeters will be presented. The problem of asymmetric velocity profiles at the exit of the test pipes was addressed and changes were made to the air delivery system to improve them. Detailed velocity profiles were taken for each test pipe and will be presented.

Further video photography providing more extensive coverage of the run matrix has been performed. A flow regime map correlating bubble behaviour at the pipe exit with pipe diameter and gas flowrate has been generated and will be presented. Also, high speed photography has been used to obtain a more accurate assessment of the bubble growth process than is possible with the video system. This should provide some quantitative data of bubble volume versus time.

Résumé

Le présent rapport est un résumé des travaux effectués à l'Université de Calgary, d'avril 1989 à mars 1990, sur la dynamique des bulles formées à la sortie de gros tuyaux immergés. Ces travaux doivent contribuer à enrichir nos connaissances de base de la dynamique des grosses bulles, nécessaires pour mieux comprendre le comportement d'une éruption d'un puits de pétrole sous l'eau, très près de la tête de puits. Le rapport tient compte à la fois d'une approche expérimentale et computationnelle du problème, et résume les progrès réalisés jusqu'à présent dans ces deux domaines.

La rapport provisorie de l'année dernière (Bugg et Rowe (1989(a)) traitait de la commande d'une installation d'essai de la dynamique des bulles et présentait quelques résultats expérimentaux préliminaires obtenus à l'aide de vidéos et de photographies. D'après les observations préliminaires, il analysait certains des phénomènes dominants qui semblent régir le comportement des grosses bulles.

Au cours de la présente période de compte rendu, certaines des lacunes identifiées lors de la commande de l'installation d'essai ont été étudiées et corrigées. Un débitmètre Venturi critique additionnel a été modifié afin d'offrir une gamme plus vaste de débits. Une forme améliorée de courbe d'étalonnage de tous les débitmètres sera présentée. Le problème des profils asymétriques des vitesses des tuyaux d'essai a été étudié, et des modifications ont été apportées au système d'alimentation en air pour améliorer les profils. Des profils détaillés des vitesses ont été pris pour chaque tuyau et seront présentés dans le cadre du présent rapport.

D'autres vidéos permettant une meilleure couverture de la matrice de passage ont été pris. Une carte du régime d'écoulement mettant en corrélation le comportement des bulles à la sortie du tuyau avec le diamètre du tuyau et le débit du gaz a été produite et sera présentée dans le cadre du texte. La photographie ultra-rapide a également été utilisée pour obtenir une évaluation du processus de croissance des bulles plus précise qu'il n'est possible d'obtenir avec le système vidéo. Cela devrait fournir certaines données quantitatives du volume des bulles par rapport au temps.

2.0 Test Facility Development

2.1 Flowmeters

The last interim report (Bugg and Rowe [1989(a)]) detailed the calibration procedure for the circular arc critical venturi meters used in this study. During this reporting period an additional meter with a throat diameter of *2.5mm* was made to compliment the existing *5mm* and *8mm* venturis. This allows lower flowrates to be achieved while still operating in the choked condition and is important since a smaller (*25.4mm*) pipe was added to the run matrix.

The calibration procedure will not be repeated here in detail. To summarize, the procedure involves directing the air flow through a straight length of pipe which is long enough to ensure fully developed turbulent flow. The mass flow through the pipe is then measured based on a single centreline measurement of the velocity. During the last year the symmetry of the flow in this long length of pipe was confirmed by a detailed pitot tube traverse. The results of this traverse are shown in figure 2.1.

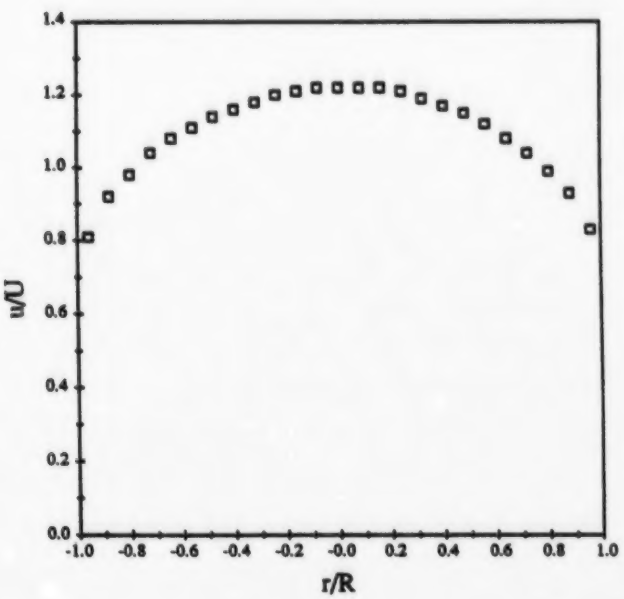

Figure 2.1: Velocity profile in the venturi meter calibration pipe.

The updated calibration data are presented in a plot of discharge coefficient versus throat Reynolds number in figure 2.2 for each of the three flowmeters. These data all falls within five percent of the correlation given by the solid line in figure 2.2 which was developed by Arnberg, Britton and Seidel [1973] for circular arc critical venturi meters.

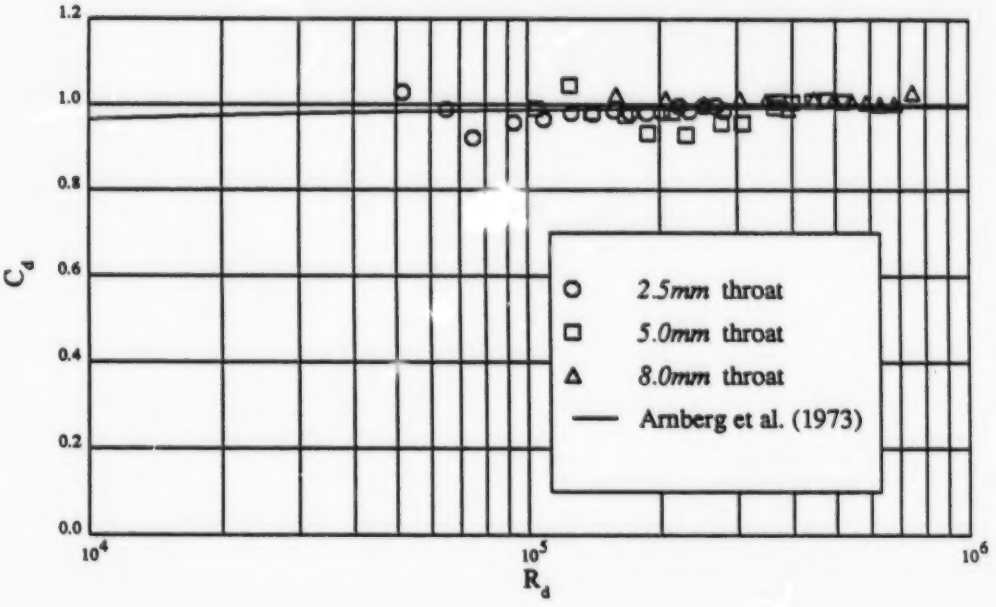

Figure 2.2: Discharge coefficient versus throat Reynolds number.

2.2 Air Flow Symmetry

Preliminary checks of the air flow symmetry at the exit of the test pipes were presented in Bugg and Rowe [1989(a)]. These indicated that for test pipes with small length to diameter ratios (L/D's) the velocity profiles were unacceptably asymmetrical. As a result, an effort was made to correct the velocity profiles by modifying the air delivery system.

Because of the unavoidably small L/D of the test pipes and the difficulty in providing any straight development length upstream of the test pipes, a trial and error procedure of testing various flow

deflection devices was adopted until acceptably symmetric profiles were obtained. The solution involved extending the inlet pipe into the small plenum chamber mounted on the bottom of the tank (see Rowe and Bugg [1988]) and perforating it with a hole pattern that would distribute the air flow into the plenum more uniformly. After several configurations were tested, one was arrived at that gave reasonably symmetric profiles for all test pipes in the run matrix.

These symmetry tests were conducted in the absence of water in the tank and consisted of pitot tube traverses across the pipe exit along eight different diameters. All four diameters (*25.4mm, 50.8mm, 76.2mm* and *101.4mm*) and both lengths (*7.6cm* and *30cm*) were tested. The resulting velocity distributions are shown in appendix A. As expected, the symmetry of the velocity profile improves as the L/D of the test pipe increases. Although not perfectly symmetrical, all test pipe velocity profiles are now considered acceptable. Most notably, regions of reverse flow at the test pipe exit have been eliminated from the very small L/D cases.

2.3 Run Matrix Revision

The additional flowmeter allows smaller gas flowrates to be reliably supplied to the test rig. As a result the minimum flow in the run matrix has been revised to *2.5 litres/sec* from *5 litres/sec*. The maximum flow of *50 litres/sec* and the pipe diameter range of *25.4 mm* to *101.4 mm* have been retained.

3.0 Flow Regime Mapping

Although last years interim report discussed various types of bubble behaviour, these phenomena were not correlated with the two main parameters of the study. This section will present a flow regime map that describes the observed behaviour as a function of pipe diameter and gas flowrate. A detailed description of each type of bubble behaviour, with photographs, can be found in Bugg and Rowe [1989(a)] or Bugg and Rowe [1989(b)]. They will be reviewed here briefly before the flow regime map is presented.

3.1 Total Backflooding

For large diameter pipes at low gas flowrates there is often such significant backflooding that no large bubbles are formed. This regime is most evident for the largest diameter pipe. No bubbles are formed at the actual pipe exit. Much smaller bubbles, probably formed at the perforated plate on the floor of the tank, rise through the flooded test pipe. As the gas flowrate is increased there is no distinct point where bubbles begin to form at the test pipe exit. At first, only occasional, small diameter toroidal bubbles form around the lip of the pipe. As the flowrate is further increased this becomes more common. At this stage there is still very significant backflooding down the centreline of the pipe but the pipe exit itself has become a definite site of bubble formation.

3.2 Single Bubbles

Over quite a narrow range of conditions, single bubbles are formed. However, in most cases the transition between severe backflooding and multiple bubble formation does not include a definite region where single bubbles are produced.

3.3 Pairing

Over a very large range of the run matrix there is a definite pairing of bubbles taking place. This process involves two different types of bubbles being formed. The first type of bubble has a spherical upper surface and appears to be relatively unaffected by the previous bubble formed. As it departs and rises, large deformations in its surface begin to grow and the second bubble begins to form at the pipe exit. As this bubble grows, its top surface points upwards toward the rear of the

first bubble. It appears to be quite heavily influenced by the flow field around the first bubble. As it departs it accelerates very rapidly upwards and is stretched along the vertical axis. It very quickly collides with the first bubble and seems to trigger complete break-up.

3.4 Larger Groups

Multiple bubble formations in groups greater than two are also observed on occasion. Sequences of three bubbles are quite common and sequences of four or five also occur. The interaction between bubbles is similar to pairing but persists for more than two bubbles at a time.

3.5 Chains

For small pipes at high flowrates no real groups occur. Each bubble seems heavily influenced by the previous one and is literally pulled from the pipe by the circulation of the previous bubble. As each bubble departs it is stretched about the vertical axis of the pipe a great deal and a continuous train of vertically elongated bubbles dominates the region just above the pipe exit.

3.6 No Backflooding

The upper bound of backflooding is at quite a high flowrate. The only cases where there is definitely no backflooding is the *25.4mm* diameter pipe at flowrates above *5 litres/sec* and the *50.8mm* diameter pipe at gas flowrates above *25.5 litres/sec*. It is obvious that a wide range of operating conditions has some degree of backflooding even when quite large bubbles are being formed. This backflooding appears primarily down the centreline of the pipe.

3.7 Flow Regime Map

The flow regime map is shown in figure 3.1. The first regime, total backflooding, dominates the upper left region of the flow regime map. In the next regime the formation of single large bubbles is dominant. In this regime a very large amount of backflooding is still observed but single large bubbles with little influence on one another are formed. As the flowrate is increased the large pairing regime becomes dominant. Most of the pairing regime also involved significant backflooding, however, some conditions exist where pairing occurs with no backflooding. This regime is also

indicated. The last regime on the map is that of multiple bubble formation where chains of bubbles that are heavily influenced by the previous bubble are dominant. No backflooding was observed in conjunction with this regime.

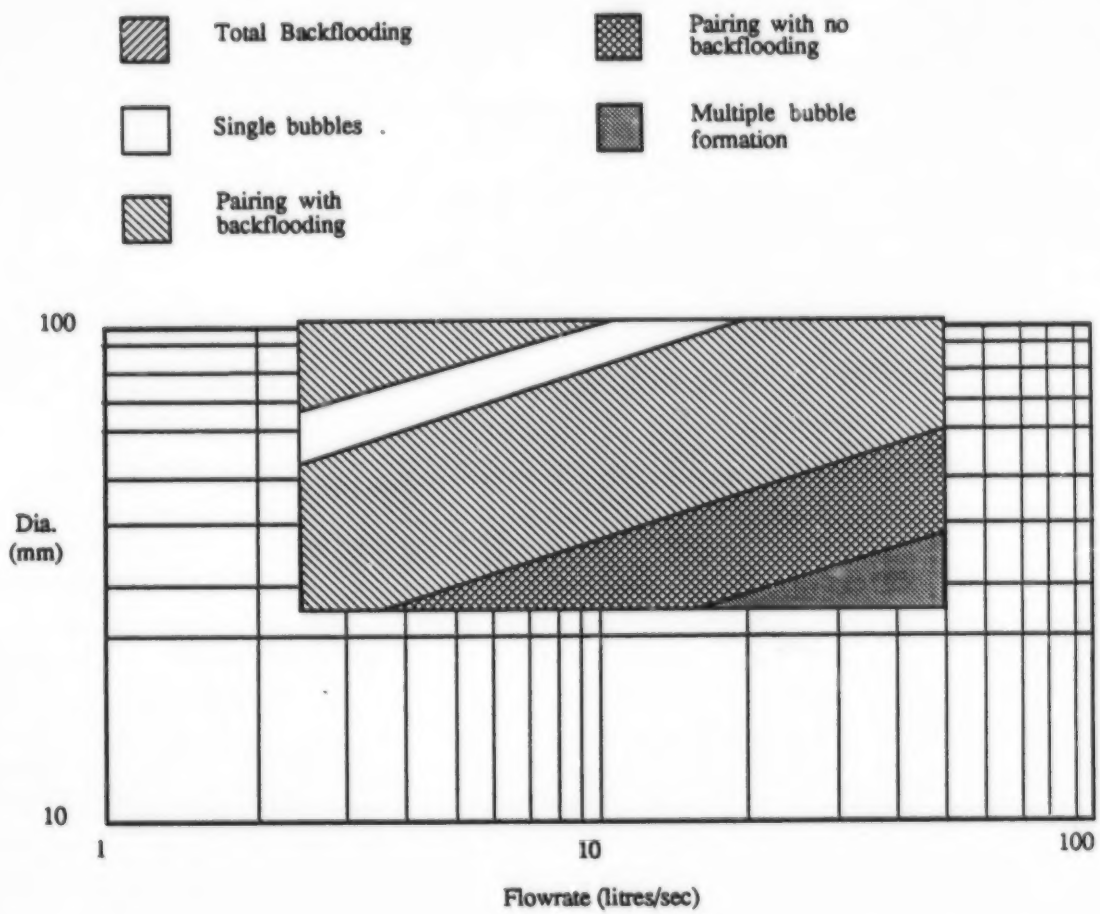

Figure 3.1: Flow regime map for large bubbles formed at submerged pipe exits.

4.0 High Speed Photography

High speed photography of growing bubbles is accomplished with a *16mm* Hycam movie camera. A framing rate of 200 pictures per second (pps) yields good time resolution of the growing bubbles over a wide range of conditions. Preliminary Hycam sequences have been taken at the run matrix locations indicated in figure 4.1.

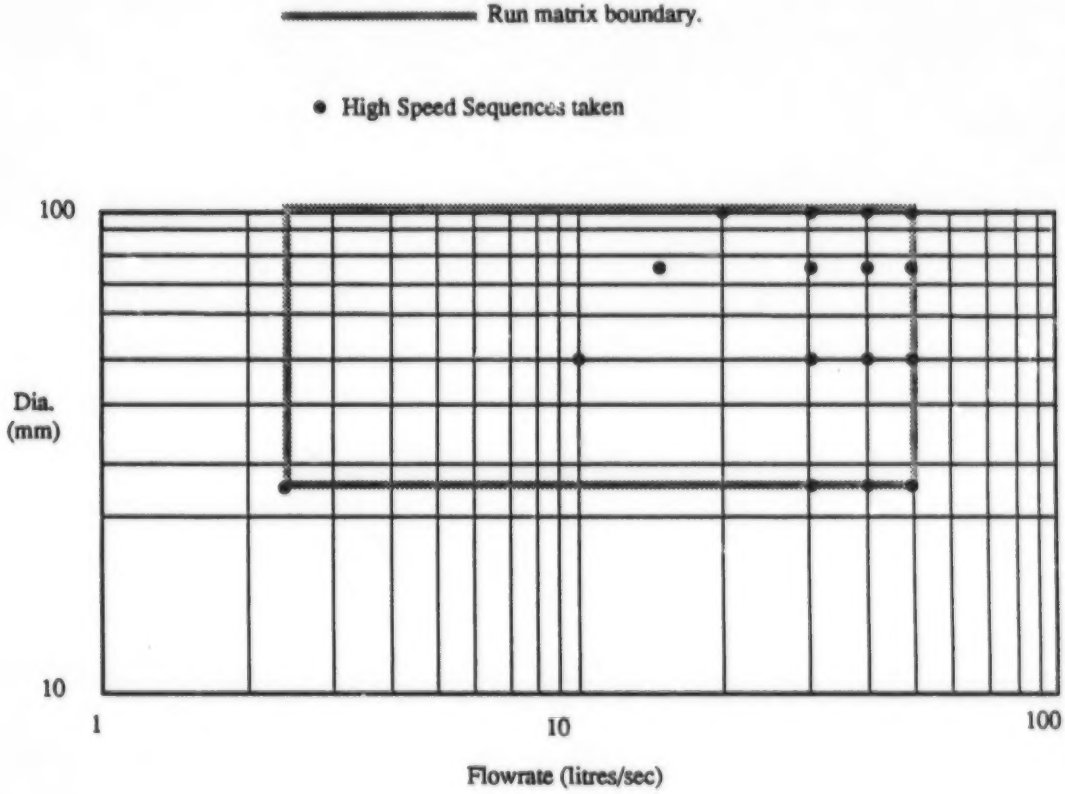

Figure 4.1: Run matrix coverage by high speed photography.

Analysis of these results is currently under way but some preliminary results will be presented here. Figures 4.2 through 4.4 show typical sequences for the conditions indicated in the figure captions.

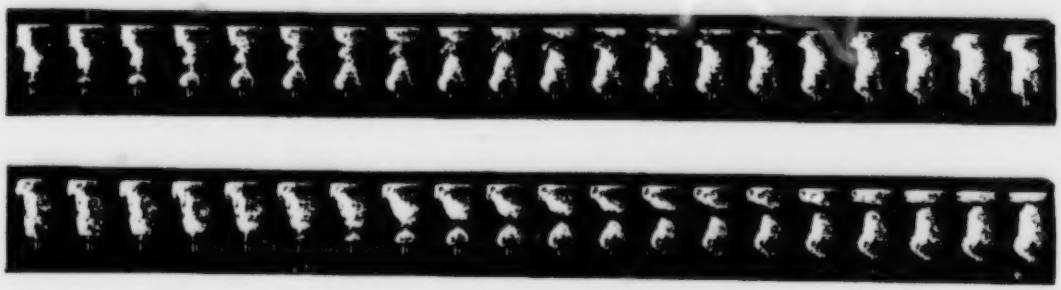

Figure 4.2: Sequence at 200pps for a 25.4mm test pipe at 40 litres/sec.

Figure 4.2 illustrates a high flowrate through a small diameter pipe. This is an example of multiple bubble formation and illustrates how every bubble formed is heavily influenced by the velocity field induced by the previous bubbles. Although each bubble initially has a spherical upper surface, it is quickly elongated upward by the influence of the flow field induced by previous bubbles. Note that, under these conditions, no backflooding occurs.

Figure 4.3 is at the same flowrate but the pipe diameter has increased to *50.8mm*. This is a good example of the pairing regime. The formation of the first bubble of a typical pair is shown near the

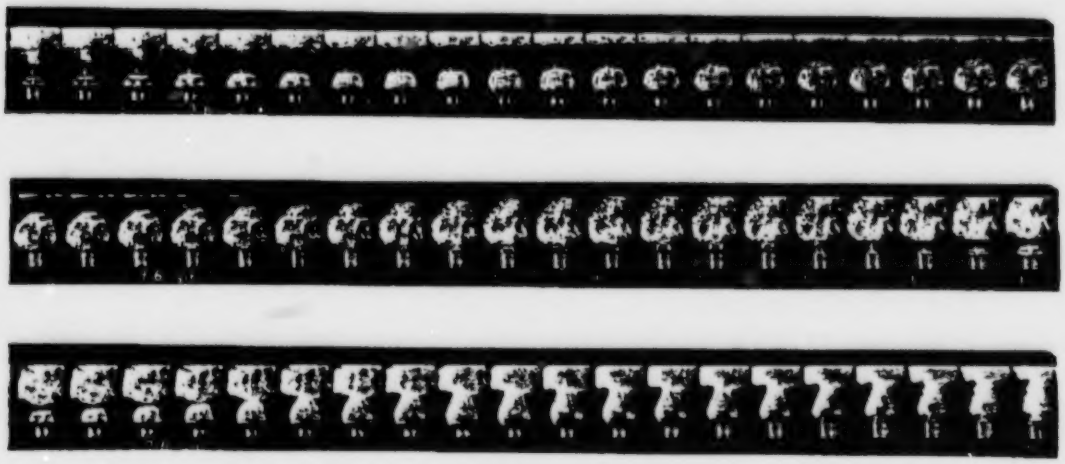

Figure 4.3: Sequence at 200pps for a 50.8mm test pipe at 40 litres/sec.

beginning of the sequence. Note that it grows as a sphere while it is still attached to the pipe. After it departs and begins to rise under the force of buoyancy, the second bubble begins to grow at the pipe exit. The influence of the first bubble on the growth of the second can be easily seen as the second is stripped from the pipe exit by the vorticity induced by the first. No backflooding is occurring under these conditions.

The flowrate in figure 4.4 is again *40 litres/sec* but now the pipe diameter is *76.2mm*. This sequence illustrates a phenomena that was not clearly illustrated by the videos. Although this is still in the pairing regime, there is apparently a small bubble formed after each of the two large bubbles. This can be clearly seen immediately after the first bubble formed is clear of the pipe exit. Reviewing figure 4.3, this can be seen to a lesser extent for the *50.8mm* pipe also.

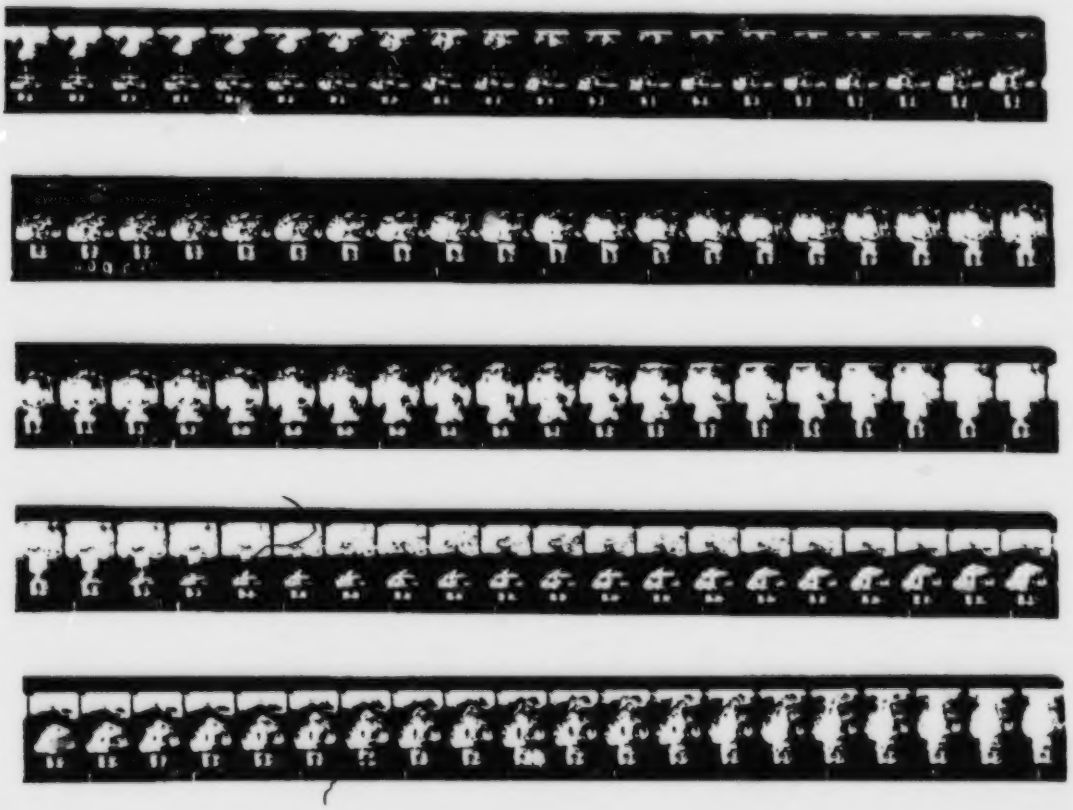

Figure 4.4: Sequence at 200pps for a 76.2mm test pipe at 40 litres/sec.

5.0 Computational Results

The computational results to date are best summarized by including a pre-print of a paper submitted to the International Journal for Numerical Methods in Fluids (see appendix B). This paper provides an overview of the model and presents the results of simulations of the initial motion of two and three dimensional isolated large bubbles in quiescent fluids. Development of the model is ongoing in an attempt to extend it to the laboratory conditions described in this report as well as conditions approximating a full scale blowout as outlined in Meikle [1981].

6.0 Conclusions

During the last year, improvements have been made in the large bubble test facility to enable a more detailed and systematic exploration of large bubble behaviour than was done in the preliminary investigations. Specifically, an additional flowmeter was constructed in order to allow lower flowrates and thereby extending the scope of the run matrix and providing better overlap with the work of previous investigators. Also, the problem of flow symmetry at the test pipe exits has been addressed and corrected. This provides a more sound basis for interpreting the observations from the experiments, especially for the large pipe diameters.

After these modifications, a more extensive series of videos were taken. High speed photography has also been used recently. It is felt that high speed photography provides a much more detailed picture of the bubble growth process. These data will be further analysed to provide a more detailed and accurate flow regime map. It may also provide some bubble volume versus time data for the period of growth when the bubble is attached to the pipe.

The computational investigation has looked extensively at the problem of the release of single bubbles in quiescent fluids. Preliminary runs of gas ejection from a pipe have also been done. In the next year the possibility of extending the model to the conditions of these experiments as well as attempting to model the initial portion of a full scale blowout will be investigated.

7.0 References

Arnberg,B.T., Britton,C.L., Seidel,W.F.: "Discharge Coefficient Correlations for Circular-Arc Venturi Flowmeters at Critical (Sonic) Flow:, Transactions of the ASME, Paper No. 73-WA-FM-8, 1973.

Bugg,J.D., Rowe,R.D.: "Report on a Large Bubble Dynamics Study", submitted to Environment Canada/Conservation and Protection, River Road Environmental Technology Centre, DSS Contract No. KE144-8-6116, March 1989(a).

Bugg,J.D., Rowe,R.D.: "An Experimental Study of Large Bubble Dynamics", Proceedings of the Twelfth Arctic and Marine Oilspill Program Technical Seminar, pp 105-114, Calgary, June 1989(b).

Meikle,K.M.: Summary of Discussion, Proceedings of a Workshop on the Sub-Sea Containment of Oil, pp115-120, Toronto, February 11-12, 1981.

Rowe,R.D., Bugg,J.D.: "Report on a Large Bubble Dynamics Study", submitted to Environment Canada/Conservation and Protection, River Road Environmental Technology Centre, DSS Contract No. KE144-7-6049, March 1988.

APPENDIX A: Air Flow Symmetry Data

This appendix contains the velocity profile data to test the flow symmetry at the exit of the test pipes. The data were taken with no water in the tank and consisted of pitot tube traverses along eight diameters as shown in figure A.1. The traverses indicated with solid lines were made over the full diameter while those shown as dashed lines were only done for $r/R > 0.5$.

Each line is identified by a symbol which is used to plot the actual data in figures A.2 through A.5 for each of the eight test pipes available.

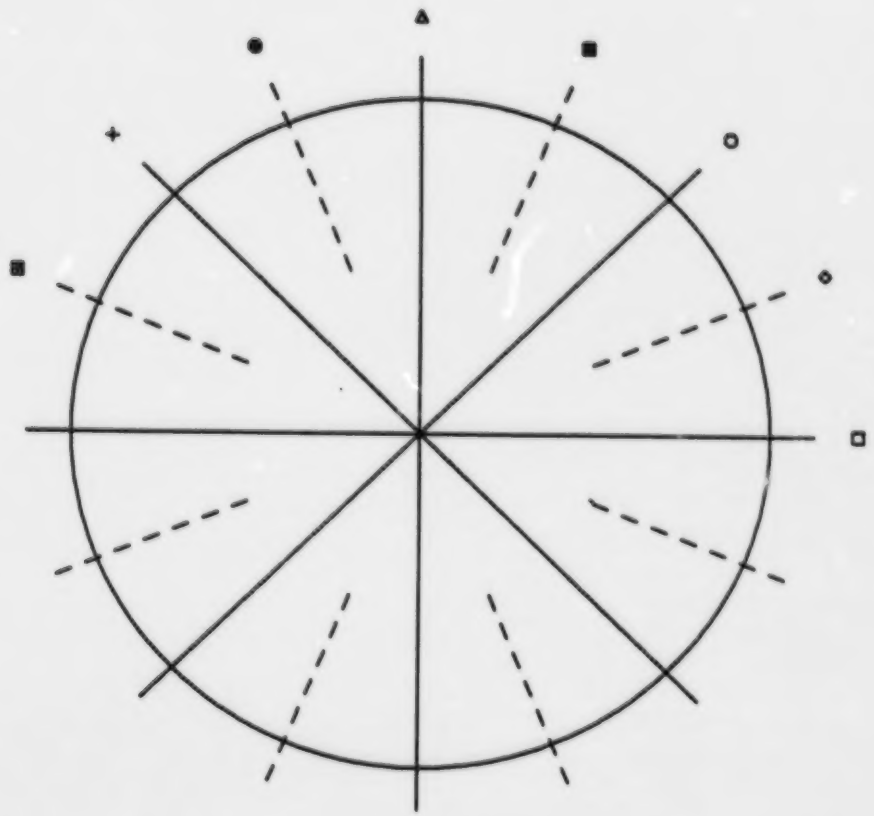

Figure A.1: Traverse positions for flow symmetry data.

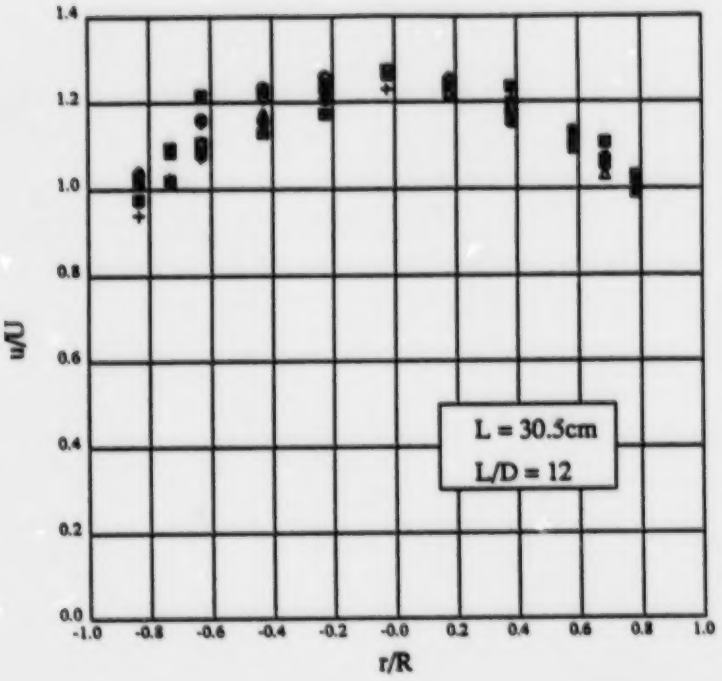

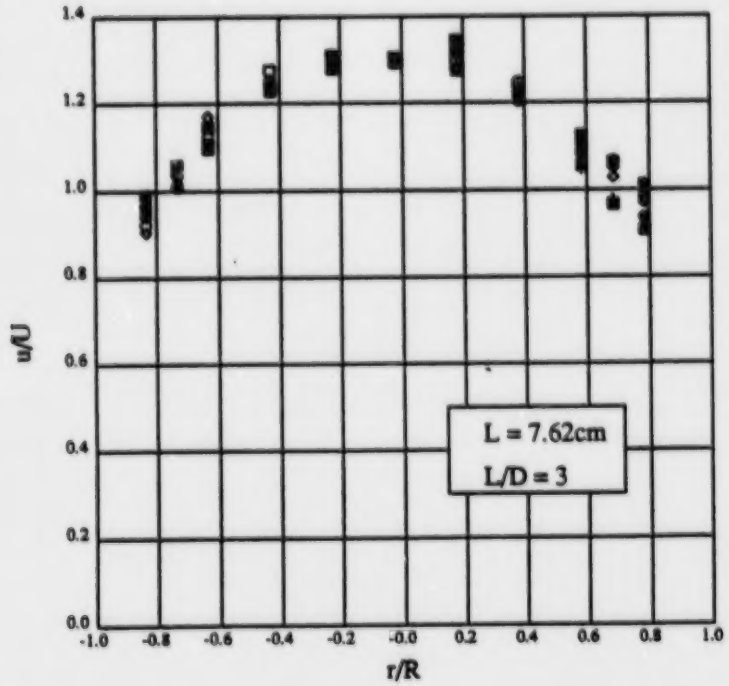

Figure A.2: Flow symmetry for 25.4 mm test pipe.

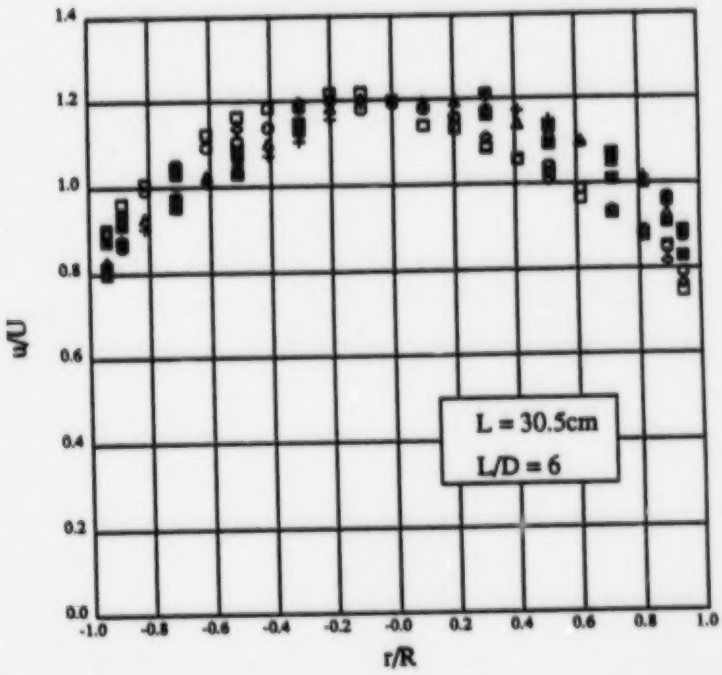

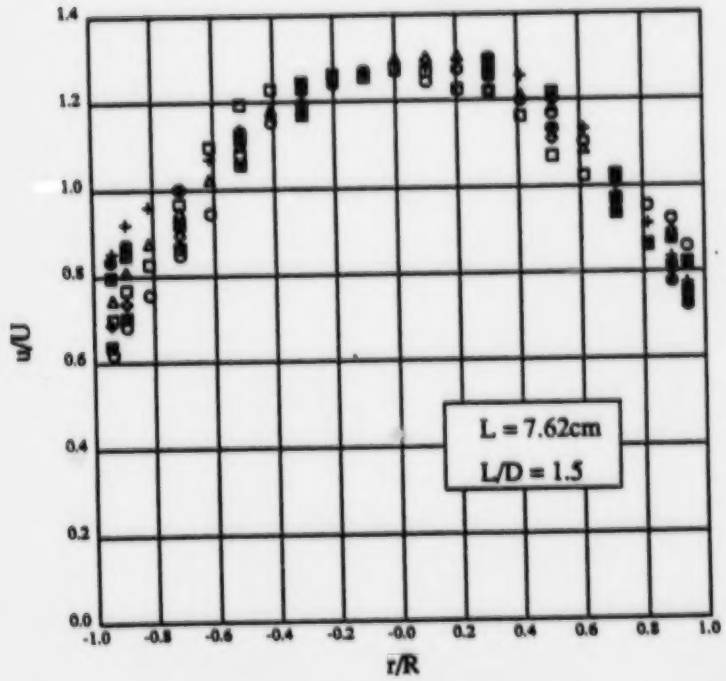

Figure A.3: Flow symmetry for 50.8 mm test pipe.

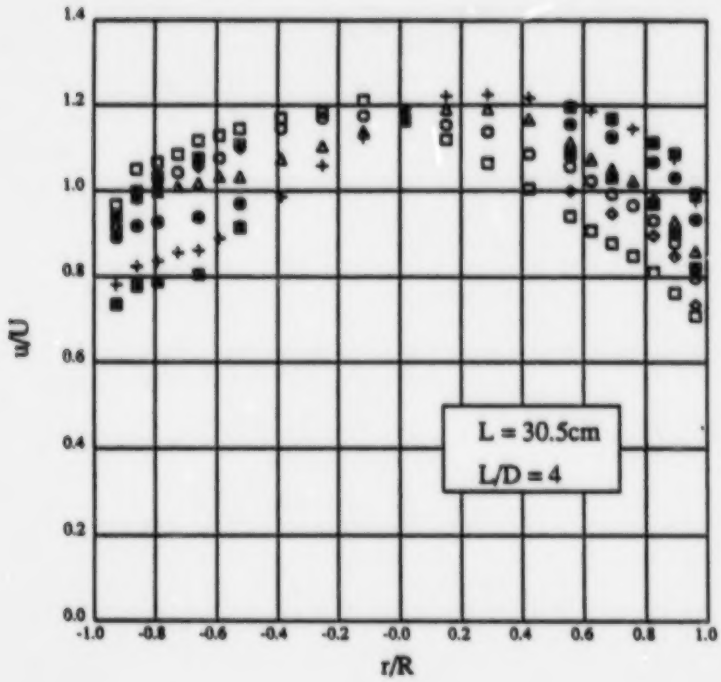

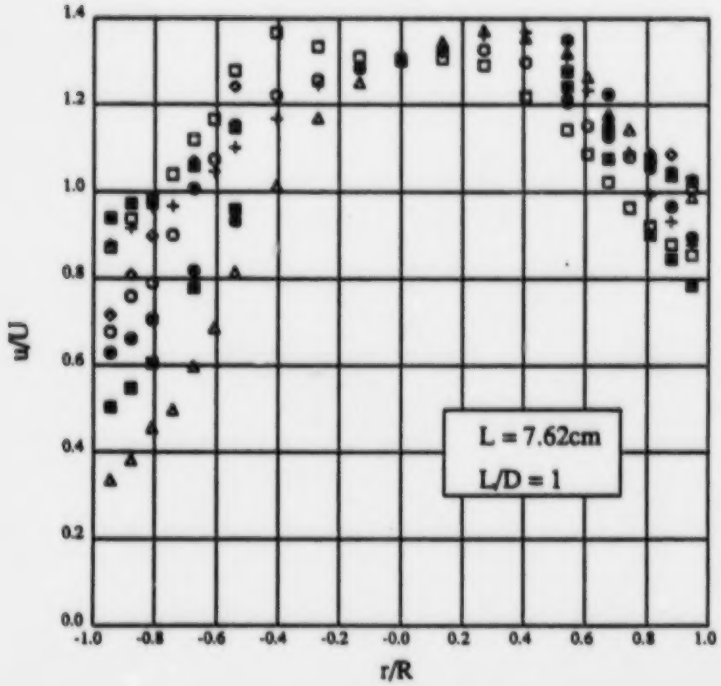

Figure A.4: Flow symmetry for 76.2 mm test pipe.

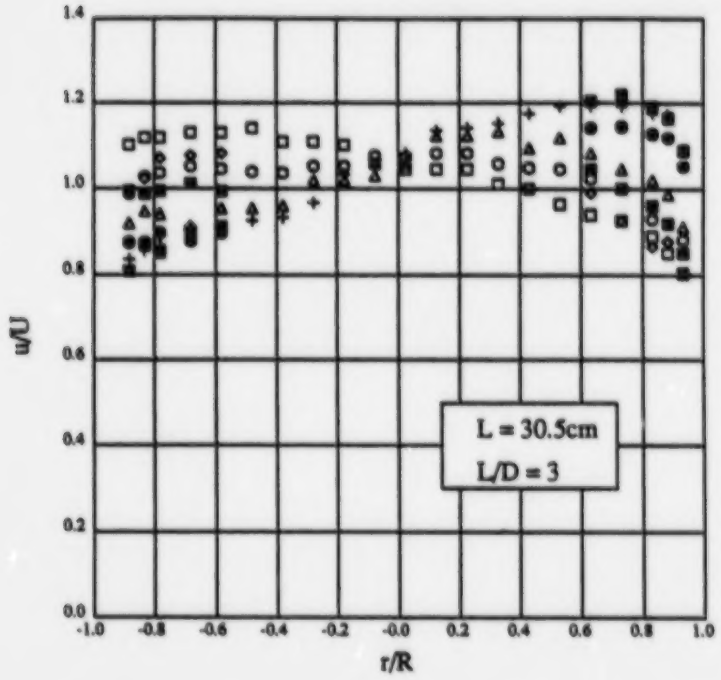

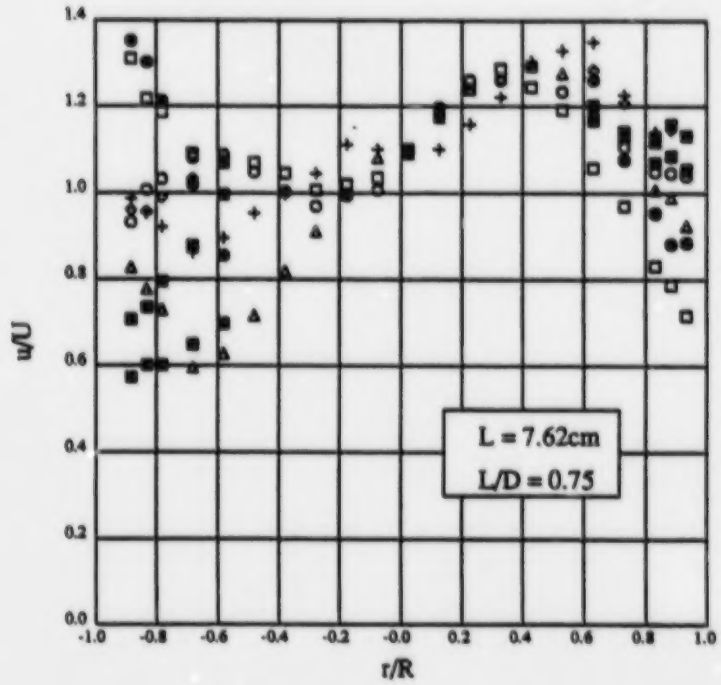

Figure A.5: Flow symmetry for 101.6 mm test pipe.

APPENDIX B:

Paper submitted to The International Journal
for Numerical Methods in Fluids

Title: Modelling the Initial Motion of Large Cylindrical and Spherical Bubbles

Authors: J.D. Bugg and R.D. Rowe

Affiliation: Department of Mechanical Engineering
The University of Calgary
2500 University Drive NW
Calgary, Alberta, Canada
T2N 1N4

Key Words: Bubbles Finite Difference Initial Motion

SUMMARY

A two dimensional, transient, finite difference technique based on a volume fraction specification of the free surface position and accounting for the effects of surface tension is shown to accurately predict the initial motion of large cylindrical and spherical bubbles. The predictions compare very favourably with the experimental data of Walters and Davidson. The initial acceleration of cylindrical and spherical bubbles is properly predicted as g and $2g$ respectively. The penetration of a tongue of liquid from below is the dominant process by which large deformations from the original shape take place and is well predicted by the model in both cases. For the spherical case, the eventual transition into a toroidal bubble is demonstrated and the circulation associated with a rising toroidal bubble as a function of its volume upon release is shown to agree very well with experiments. Iterative linear equation solving techniques applicable to the special nature of the linear system resulting from such a free surface specification are surveyed and a simple Jacobi iteration based on red-black ordering is found to perform well. The impact of the free surface on relaxation of the linear system and the convergence criteria is also explored.

INTRODUCTION

Like most numerical work requiring "large" digital computers, the study of bubble dynamics in the numerical laboratory is a relatively recent frontier in fluid dynamics. Earlier efforts to study this important class of free surface flows have been largely confined to experimental and analytical studies. In this paper, interest is focused on the initial motion of cylindrical and spherical bubbles released from rest in quiescent fluids. Furthermore, these bubbles are considered large (> 1cm dia) and undergo substantial deformations shortly after release. Some experimental data are available against which the model's performance can be evaluated.

The bubble dynamics literature is very extensive because of the importance of bubbles in many chemical and heat transfer processes. However, research has been largely confined to rather small bubbles (< 5mm dia) where surface tension and viscous effects are very important; e.g. Harper[1]

provid s a comprehensive review of small bubble behaviour. As the bubble's radius, a_o, increases, buoyant forces become more dominant and the hydrostatic pressure gradient becomes important. This paper deals with large air bubbles in water where the Eotvos number E = 100–1000. Large bubbles are relatively unstable due to the rapid growth of disturbances on their surfaces. They are of interest in such applications as underwater detonations[2,3], fluidised beds[4], nuclear reactor accident analysis[5,6] and the blowout of undersea oil-wells.[7]

In order to place the existing literature and current research in context, consider the three stages of motion of a large cylindrical bubble released from rest in a quiescent liquid. Initially, the bubble accelerates upwards under the force of buoyancy with little change from its original cylindrical shape. During the second stage it undergoes large deformations until it forms a cylindrical cap (and, perhaps, some small satellite bubbles) which eventually rise at some steady velocity during the final stage. Large spherical bubbles behave similarly but produce a spherical cap and/or a toroidal bubble in the final flow stage. This paper is concerned with the motion of large bubbles during the first and second stages. No attempt is made to model steady cylindrical or spherical cap bubbles.

Experimental Literature

The experiments most relevant to this paper are those of Walters and Davidson[8] concerned with cylindrical bubbles and those of Walters and Davidson[9] dealing with spherical bubbles. They provide position and deformation data versus time for the initial stages of motion. As well, they contain photographs of the bubbles well into the large deformation stage. These works provide the primary source of experimental data against which the model will be compared and as such will be discussed in more detail later.

Davies and Taylor[10] were the first to explain the observed spherical upper surface of spherical cap bubbles as a balance between the dynamics of the flow and gravity which preserves the constant pressure condition. Experiments with rising spherical cap bubbles led to the relationship $U = 2/3\sqrt{ga}$ for the terminal velocity of spherical cap bubbles. Studies of the wake structure behind steadily rising

cylindrical and spherical cap bubbles have been reported in several papers such as Lindt[11,12], Crabtree and Bridgewater[13], and Collins.[14] Bessler and Littman[15] produced cylindrical cap bubbles by the same technique as Walters and Davidson[8] but report no data until the terminal velocity had been reached. However, the steady flow stage focused on in these works is not the main interest, or strength, of the current model.

Several papers dealing with large bubble dynamics examine the continuous ejection of gas from a submerged orifice. This is a much more complicated problem because it contains a bubble growth process, a departure process and significant bubble to bubble interaction. However, since the large bubble literature is quite limited the work of Chen and Dhir[6], Topham[7] and Marble et al.[5] should also be mentioned here.

Theoretical Literature

The most noteworthy theoretical treatment of the initial motion of large bubbles is the work of Walters and Davidson.[8,9] Their analysis is based on defining the velocity potential for flow around a cylindrical/spherical bubble. This velocity potential is an infinite series, with the first term being the well known potential for a solid cylinder/sphere in a uniform stream. The remaining terms of the series have time dependent coefficients. The basis of their method is to determine these coefficients such that the condition of uniform pressure at the bubble surface is satisfied. They found that the initial acceleration of a cylindrical bubble released from rest is g while for a spherical bubble it is $2g$. Also, a tongue of liquid is found to penetrate the bottom of the bubble. Because of the truncation of the infinite series defining the velocity potential, the analysis is only valid for small deviations from the original shape or until the bubble moves about one bubble radius.

Virtually every other theoretical treatment of large bubble dynamics is concerned with the terminal velocity or wake structure of cylindrical and spherical cap bubbles. Since these are concerned only with the final, steady stage of motion, individual contributions will not be detailed here. A review of these phenomena has been provided by Wegener and Parlange.[16]

Numerical Literature

Numerical investigations of large bubble movement through liquids are quite recent. Several approachs are apparent in the literature. The first is the vortex-in-cell method. This technique has evolved from the original Lagrangian vortex interaction calculations of Rosenhead[17] to the modern vortex-in-cell technique where the vortex elements are moved by solving the stream function vorticity equation on an underlying grid. The use of an underlying grid requires only $O(N \ln N)$ operations per time step whereas the original technique of summing over each vortex element requires $O(N^2)$ operations per time step[18] (N being both the number of cells and the number of vortex elements since they are of the same order for simulations with highly distorted surfaces). In bubble calculations the density interface is represented by a series of point vortices whose strength is determined by the vorticity generating misalignment of the pressure and density gradients. Simulations by Brecht and Ferrante[19] and previously by Meng and Thomson.[20] chronicle an impressive range of bubble movement predictions, including important studies of various bubble to bubble interactions. However, they consider quite low density ratios (maximum $\rho_1/\rho_2 = 32$) while the current research is concerned with air water simulations where $\rho_1/\rho_2 = 1000$.

Another approach is boundary fitting finite difference techniques where an orthogonal grid is generated to give a constant coordinate value on the bubble surface. This formulation makes the free surface boundary condition relatively simple to apply since coordinate lines are perpendicular to the surface and all control volumes are either completely full or completely empty. Ryskin and Leal[21,22] describe such a technique applied to the steady flow around a spherical cap bubble using a stream function vorticity formulation. They restricted their study to the steady flow stage and therefore did not model the initial stages of motion. The maximum Reynolds number considered was 200.

An alternative approach, used in this paper, makes no attempt to fit the coordinate system to the bubble surface but allows the free surface to assume any orientation relative to the coordinate lines. This makes the free surface boundary condition more difficult to assign and results in some partially full control volumes. The SOLA-VOF code[23] descended from the MAC[24] (Marker and Cell) technique

uses this approach. The advantages are more generality in the free surface configuration and elimination of the curvilinear orthogonal grid as an unknown in the solution. The difficulties arise in convecting the free surface position in a physically realistic manner.

ANALYSIS

The model in this paper uses the SOLA-VOF[23] approach to determine the position of the air/water interface. It is a finite difference technique which advances explicitly in time and uses a pressure correction technique to drive $\nabla \cdot \vec{u}$ to zero. All simulations in this paper were done on a uniform grid ($\delta x = \delta y = constant$).

Full control volumes

The following discretised form of the Navier-Stokes equations is used.

$$u_{ij}^{n+1} = u_{ij}^{n} - \delta t C_{x_{ij}}^{n} - \delta t V_{x_{ij}}^{n} - \frac{\delta t}{\delta x \rho} \left(P_{i+1,j}^{n+1} - P_{ij}^{n+1}\right) \tag{1}$$

$$v_{ij}^{n+1} = v_{ij}^{n} - \delta t C_{y_{ij}}^{n} - \delta t V_{y_{ij}}^{n} - \frac{\delta t}{\delta y \rho} \left(P_{i,j+1}^{n+1} - P_{ij}^{n+1}\right) \tag{2}$$

The convective terms have been grouped into C_{ij} and the viscous terms have been grouped into V_{ij}. The viscous terms are always central differenced while the differencing scheme for the convection term is varied between central and upwind differencing depending upon the strength of the convection. This equation set is not closed because continuity has not yet been imposed. This is done by first estimating the velocity field and then correcting it by adjusting the pressure field to satisfy continuity. Details of this process can be found in Rowe and Bugg.[25] The result is a linear equation for the pressure correction terms.

$$\Delta P_{ij} - \frac{\Delta P_{i-1,j}}{2(1+(\frac{\delta x}{\delta y})^2)} - \frac{\Delta P_{i+1,j}}{2(1+(\frac{\delta x}{\delta y})^2)} - \frac{\Delta P_{i,j-1}}{2(1+(\frac{\delta y}{\delta x})^2)}$$

$$- \frac{\Delta P_{i,j+1}}{2(1+(\frac{\delta y}{\delta x})^2)} = - \frac{\rho D_{ij}^{\delta} \delta x^2 \delta y^2}{2 \delta t (\delta x^2+\delta y^2)} \tag{3}$$

This equation can be written for each control volume in the solution domain and contains five unknown pressure corrections.

Surface control volumes

The above procedure is valid only for control volumes that are full of liquid. Since this code has the capability of tracking free surfaces, control volumes containing free surfaces must apply the free surface boundary condition in the interior of the solution domain. The free surface boundary condition is

$$\frac{\partial s_{nn}}{\partial \hat{n}} = 0 \tag{4}$$

where $\hat{n}$ is normal to the free surface and s_{nn} is the normal stress in that direction. At the surface this means that

$$P_g + \kappa\sigma = P_l + \mu\frac{\partial u_n}{\partial n} \tag{5}$$

where P_g = the bubble gas pressure, κ =the local surface curvature, σ = surface tension and P_l = the liquid side pressure. However since,

$$\frac{\kappa\sigma}{\mu\frac{\partial u_n}{\partial n}} = O(\frac{\sigma}{\mu U}) = O(\frac{\sigma}{\mu\sqrt{g a_o}}) = O(100) \tag{6}$$

the viscous term can be neglected giving,

$$P_l = P_g + \kappa\sigma \tag{7}$$

The goal is to set the surface cell pressure such that it will result in a surface pressure of P_l when linearly interpolated to the neighbouring full cell (see figure 1). We want,

$$P_{ij}^{n+1} = \eta_{ij} P_l + (1-\eta_{ij}) P_{pq}^{n+1} \tag{8}$$

However, the linear system is in ΔP so to express (8) in a form consistent with full cells it is written as,

$$\Delta P_{ij} + (\eta_{ij} - 1)\Delta P_{pq} = \eta_{ij} P_s + (1-\eta_{ij}) P^a_{pq} - P^a_{ij} \tag{9}$$

The solution of (3) and (9) is the largest task facing the model. Several techniques have been pursued in light of the special problems imposed by the free surface. The first influence of equation (9) is that it renders the coefficient matrix asymmetric. This increases the storage requirements greatly and rules out solvers which rely on symmetric coefficient matrices. The second and most serious consequence of (9) is that it introduces severe numerical instabilities when η_{ij} is greater than two by violating diagonal dominance. A full discussion of the solution techniques implemented in light of these problems is provided below.

Convecting the Free Surface

The free surface position is defined in terms of a volume fraction, F, which is unity in full control volumes, zero in empty control volumes and intermediate values in surface control volumes. The process of updating F at the end of each time step convects the free surface and is governed by:

$$\frac{\partial F}{\partial t} + u\frac{\partial F}{\partial x} + v\frac{\partial F}{\partial y} = 0 \tag{10}$$

Numerical interpretation of this equation must ensure that the interface remain sharply defined and therefore a special donor-acceptor method is used. A good discussion of this technique can be found in Nichols and Hirt.[26]

Stability Considerations

The linear interpolation which specifies the free surface boundary condition can lead to a numerical instability when iteratively solving the linear equation set. If η_{ij} is greater than two diagonal dominance will be lost causing the iterative scheme to diverge. In this work a relaxation factor of $\omega_{pq} = 0.9/(\eta_{ij}-1)$ is applied to all cells where $\eta_{ij} > 2.0$. Note that since it is the ΔP_{pq} coefficient and not the ΔP_{ij} coefficient that creates the instability, the relaxation is applied in cell pq. All other cells are not relaxed in this solution.

Ordering Schemes

A large portion of the computational effort is the solution of equation 3 and 9 for the pressure correction, ΔP. Equation 3 has five non-zero members in each row of the coefficient matrix. The structure of the coefficient matrix is dependent on the ordering scheme.[27] Figure 2 shows a very small grid, ($nx = 7$, $ny = 6$), with the control volumes numbered according to three different ordering schemes. By using ordering schemes to change the structure of the coefficient matrix, more efficient iterative techniques may be implemented.

Natural Ordering: First consider natural ordering. Since the differencing molecule yields only five unknowns per equation and the order of the set is typically 10^4, the coefficient matrix is obviously very sparse. For a nx by ny grid, all elements of a_{ij} are zero except when $j=i$, $j=i-1$, $j=i+1$, $j=i-nx$, and $j=i+nx$. Therefore, A has a tridiagonal structure and an extra band of non-zero members at a half bandwidth of nx.

$$A\ \Delta P = b \tag{11}$$

Because equation 3 is normalised, the diagonal members of A are all unity.

Red-black Point Ordering: When the coefficient matrix is constructed using red-black point ordering it may be partitioned as shown in equation 12.

$$\begin{bmatrix} I & G_b \\ G_r & I \end{bmatrix} \begin{bmatrix} \Delta P_r \\ \Delta P_b \end{bmatrix} = \begin{bmatrix} b_r \\ b_b \end{bmatrix} \tag{12}$$

The sub-matrices on the diagonal are identity matrices and G_b and G_r each have four non-zero members per row. Because of this partitioning, the solution vector, ΔP, is also partitioned into ΔP_r and ΔP_b, the red and black solutions. This ordering scheme derives its name from the checkerboard-like pattern that the two solutions create. The structure of the partitioned coefficient matrix arises from the fact that no red control volume has another red control volume as its neighbour. Therefore, each half of the solution is explicit and they are linked through G_r and G_b.

Red-black Line Ordering: Red-black line ordering allows a similar partitioning (equation 13) but H_r and H_b are tri-diagonal matrices and G_r and G_b each have only two members per row.

$$\begin{bmatrix} H_r & G_b \\ G_r & H_b \end{bmatrix} \begin{bmatrix} \Delta P_r \\ \Delta P_b \end{bmatrix} = \begin{bmatrix} b_r \\ b_b \end{bmatrix} \tag{13}$$

Each half of the solution can be solved by a fast direct method (tri-diagonal matrix algorithm) and it is linked more weakly with the other half of the solution since G_r and G_b each have only two members per row.

Basic Iterative Methods

Now that the ordering schemes have been discussed, some basic iterative methods can be introduced. Not all of these basic iterative methods are used with all possible ordering schemes but several combinations are discussed and compared in this paper.

Jacobi Iterative Scheme: The simplest of all iterative schemes is the Jacobi iterative technique shown in equation 14. Every member of the solution is updated based entirely on the solution at the previous iteration. The disadvantage of this technique is that its explicit nature leads to rather slow convergence. However, in terms of vectorisation it is very attractive since it is directly vectorisable. The tradeoff between poor convergence properties and amiability to vector hardware will determine this method's utility.

$$\Delta P^{m+1} = b - (A - I)\,\Delta P^{m} \tag{14}$$

Gauss-Seidel Iterative Scheme: The next technique is the Gauss-Seidel iterative scheme. In this scheme, two of the four neighbour terms in each equation are evaluated at the current iteration. This makes it converge much more quickly than the Jacobi technique since it is more implicit. However, it is much less suitable for vectorisation because of its recursive nature. It is a very attractive method on scalar hardware using the natural ordering scheme since it merely involves stepping through the grid and updating the solution based on the current state of the solution vector.

$$\Delta P^{m+1} = (I + C_L)^{-1}(b - C_U \Delta P^{m}) \tag{15}$$

where: C_L = *lower triangular portion of A.*

C_U = *upper triangular portion of A.*

Tri-diagonal Matrix Algorithm: The tri-diagonal matrix algorithm (TDMA) is not in itself an iterative technique. It is a direct solver of a special class of linear systems having tridiagonal coefficient matrices. However, if we make each iteration a tridiagonal problem by moving the contribution of two neighbours into the constant vector, an iterative technique can be developed that has good convergence properties for many problems. Equation 16 describes this method.

$$\Delta P^{m+1} = K^{-1} (b - C_g \Delta P^m) \tag{16}$$

$$where: A = K + C_g$$

$$K = tridiagonal\ portion\ of\ A.$$

Information is transmitted along the lines that define the TDMA in one iteration whereas information is transmitted across the TDMA lines at a rate of one grid cell per iteration. Therefore, alternating the sweeping direction usually speeds up the solution substantially.[28]

Speed Comparison

To compare the speed of the five solvers, the case of a cylindrical bubble released from rest is used. A complete description of these simulations is presented in the next section. The solution domain is 61 by 160 control volumes resulting in a matrix of order 9760 and the first 25 time steps are benchmarked to produce the following table. The convergence criteria, ε, for these runs is 10^{-6} and the time step is 0.0002 second. Quantities in square brackets,[ ], are relative to the Jacobi scheme with red-black ordering(method IV in table 1).

Method	Ordering	Basic Iterative Technique	Set-Up Time (ms)	Time per Iteration (ms)	Floating Pt. Ops. per Iteration	Rate (MFLOPS)	Total Iterations	Total Time (sec)
I	Natural	Jacobi	1.69 [0.31]	2.04 [1.33]	165,920 (17N)	79.0	75121 [17.1]	152.9 [22.2]
II		Gauss-Seidel	2.94 [0.55]	10.93 [7.14]	224,480 (23N)	20.5	2488 [0.56]	27.26 [3.96]
III		TDMA	8.16 [1.52]	3.84 [2.51]	283,040 (------)	73.7	2777 [0.63]	10.87 [1.58]
IV	RB Point	Jacobi	5.38 [1.00]	1.53 [1.00]	131,760 (13.5N)	86.7	4404 [1.00]	6.883 [1.00]
V	RB Line	TDMA	8.89 [1.65]	3.41 [2.23]	200,080 (------)	58.7	2262 [0.51]	7.946 [1.15]

TABLE 1: Speed comparison of five linear equation solvers.

The set-up time in table 1 includes such things as zeroing the solution vector(s), initialising bit mask vectors for full cells and red-black cells if applicable, loading the relaxation vectors, pre-relaxing the coefficient matrix and constant vector and loading vectors required for the convergence check. For

those techniques which use the tri-diagonal matrix algorithm, the set-up time includes the coefficient matrix decomposition stage and this explains the large set-up times for methods III and V.

The time per iteration column includes both the solution and convergence check stages. Methods using the easily vectorisable Jacobi iterative technique (I and IV) are the fastest running. Two factors give rise to the differences between methods I and IV. Method IV is made slightly slower by the fact that the vector length is half that of method I. However, this is more than offset by the fact that the convergence check is usually half as large for method IV. The large time for method II results from the solution stage being only 50% vectorised (the convergence check is 100% vectorised).

The floating point operations per iteration are obtained by counting the operations in the iteration loop of the solver. The actual tri-diagonal matrix solver used in methods III and V is from the Magev[29] library of subroutines and the number of floating point operations do not vary linearly with N as for the other methods. The rate in MFLOPS is simply calculated from the time per iteration and the number of operations. A two pipe Cyber 205 was used for this study and with no linked triads, the maximum speed realisable using single precision is 100 MFLOPS. Degradation of this rate is due to vectorisability of different methods, vector set-up time and scalar overhead such as incrementing the iteration counter and deciding whether to iterate again.

A favourable method must not only be able to complete an iteration quickly, but it must also be able to obtain a converged solution in a competitive number of iterations. These two factors combine to yield the total time for this particular benchmark solution. Whereas the running speed of each method is basically independent of the case being run, the number of iterations required may depend heavily on the details of the problem being solved. The code is structured so that the assembly of the coefficient matrix and constant vector is independent of the solution method selected. This makes it very easy to change solution methods. This capability is strongly recommended since different solvers may perform better in different cases. Based on this study the favoured method for this application is the Jacobi iterative technique based on the red-black point ordering scheme.

Relaxation Technique

Methods I, II and IV use pre-relaxation to slighdy reduce the number of floating point operations inside the iteration loop. Pre-relaxation is the practice of performing a portion of the relaxation procedure before the solution by relaxing the coefficient matrix and constant vectors. Illustrating this with method I:

Post-relaxation

$$\Delta P^{m+\frac{1}{2}} = b - [(A - I)]\Delta P^{m} \tag{17}$$

$$\Delta P^{m+1} = \omega\Delta P^{m+\frac{1}{2}} + (1-\omega)\Delta P^{m} \tag{18}$$

Pre-relaxation

$$\Delta P^{m+\frac{1}{2}} = [\omega b] - [\omega(A - I)]\Delta P^{m} \tag{19}$$

$$\Delta P^{m+1} = \Delta P^{m+\frac{1}{2}} + (1-\omega)\Delta P^{m} \tag{20}$$

The quantities in square brackets, [ ], can be calculated before iteration begins. Therefore, inside the iteration loop, this technique saves one floating point operation per control volume, namely the $\omega\Delta P^{m+\frac{1}{2}}$ product in equation 18.

Convergence Criteria

A problem with iterative linear equation solvers is deciding when to stop the iteration procedure and accept the current solution. This decision demands a large part of the total time of many iterative techniques. Also, the presence of relaxation factors in the solution must be accounted for by the convergence criteria. To illustrate the formulation of the convergence criteria consider the Jacobi technique based on red-black point ordering and using the pre-relaxation technique.

$$\Delta P_r^{m+\frac{1}{2}} = \omega_r b_r - \omega_r G_b \Delta P_b^{m} \tag{21}$$

$$\Delta P_r^{m+1} = \Delta P_r^{m+\frac{1}{2}} + (1-\omega_r)\Delta P_r^{m} \tag{22}$$

$$\Delta P_b^{m+\frac{1}{2}} = \omega_b b_b - \omega_b G_r \Delta P_r^{m+1} \tag{23}$$

$$\Delta P_b^{m+1} = \Delta P_b^{m+\frac{1}{2}} + (1-\omega_b)\Delta P_b^{m} \tag{24}$$

Assume that $\Delta P = [\Delta P_r^{m+1}, \Delta P_b^m]^T$ represents a converged solution. Then the residuals can be calculated from,

$$\Delta P_r^{m+1} = b_r^{m+1} - G_b \Delta P_b^m \tag{25}$$

$$\Delta P_b^m = b_b^{m+1} - G_r \Delta P_r^{m+1} \tag{26}$$

where b_r^{m+1} and b_b^{m+1} should ideally equal b_r and b_b. Multiplying 25 and 26 by ω_r and ω_b respectively, subtracting from 21 and 22 and recalling the definition of b_r and b_b gives,

$$\Delta P_r^m - \Delta P_r^{m+1} = \frac{\omega_r}{(1-\omega_r)} \frac{\rho\, \delta x^2\, \delta y^2}{2\, \delta t\, (\delta x^2 + \delta y^2)} (D_r^g - D_r^{m+1}) \tag{27}$$

$$\Delta P_b^m - \Delta P_b^{m+1} = \frac{\omega_b\, \rho\, \delta x^2\, \delta y^2}{2\, \delta t\, (\delta x^2 + \delta y^2)} (D_b^g - D_b^{m+1}) \tag{28}$$

The difference on the right hand side of this expression is the error in divergence at the $m+1$ iteration. This can now be compared with the allowable relative volume flow imbalance, ε to give the convergence criteria.

$$|\Delta P_r^{m+1} - \Delta P_r^m| < \frac{\varepsilon\, \rho\, \delta x^2\, \delta y^2\, \omega_r}{2\, \delta t^2\, (1-\omega_r)\, (\delta x^2 + \delta y^2)} \tag{29}$$

$$|\Delta P_b^{m+1} - \Delta P_b^m| < \frac{\varepsilon\, \rho\, \delta x^2\, \delta y^2\, \omega_b}{2\, \delta t^2\, (\delta x^2 + \delta y^2)} \tag{30}$$

The red-black ordering scheme makes it possible to save computation time during the convergence check. Note that 29 is certain to be satisfied in any control volume where $\omega = 1$. Therefore, criteria 30 is checked first and only if it is satisfied is there any need to check 29. This means that until very close to convergence only half of the solution needs to be checked for convergence.

Note that the convergence check described above is fully vectorisable. However, since only one control volume need violate the convergence criteria in order to demand another iteration, it may seem more efficient to do a fully scalar convergence check and proceed to the next iteration upon the first violation. Near the beginning of the iterative process where many control volumes violate the criteria this would undoubtably be faster. However, near convergence when only a few stubborn residuals remain it depends on where they are positioned in the solution vector as to which method would be

fastest. This is impossible to predict "a priori" in any general way so the fully vectorised convergence check is retained.

The fact that this code must evaluate the void fraction in each control volume in order to track the movement of the free surface places extra importance on knowing the error in the solution. The routine which updates the void fraction in each control volume at the end of each time step does so by calculating the imbalance of mass flux across the control volume faces. The convergence criteria allows a small imbalance in mass flow to occur. This allowable divergence must be considered in updating the void fraction or new, fictitious void regions may appear merely by virtue of non-zero divergence. Therefore, the minimum void fraction, α_{min}, which is allowed to appear in a previously full cell is ε.

RESULTS AND DISCUSSIONS

Cylindrical bubbles

The experiments performed by Walters and Davidson[8] provide a good test of the model's capabilities. The initial conditions are achieved by suddenly withdrawing a 50.8mm diameter sleeve from between two vertical Perspex plates 9.5mm apart, 254mm wide and 1.2m high. The computational domain covers the entire width of the tank but is restricted in height to 0.3387m resulting in a 61x160 grid having $\delta x = \delta y = 2.11\overline{6}$mm. The rather narrow width of the column in these experiments is far from the assumption of an infinite expanse of fluid. Studies show that the terminal velocity is reduced by decreasing the channel width,[14] but no work is available on their influence during the initial stages of motion. Walters and Davidson[8] state that the initial bubble pressure is set so that there is "minimal tendency for a volume change to occur on release". This is achieved in the model by initialising the bubble pressure to be equal to the hydrostatic pressure at the bubble centroid at $t=0$. Thereafter, the bubble pressure is recalculated at each time step according to the isentropic expansion/compression of air in response to changes in bubble volume resulting from updating the surface position. The present work is only intended to model the first two stages of bubble motion since the experimental data[8] is

restricted to these stages.

Initial Stage: During the initial non-deforming motion, the most important quantity to verify is the bubble's acceleration. This can be shown theoretically, and has been confirmed experimentally[8] , to be equal to the gravitational acceleration, g. Figure 3, which shows the bubble position versus time obtained from Walters and Davidson[8] , confirms that the model properly predicts this initial acceleration. Note that for $T = t\sqrt{g/a_o} > 1.0$ the upward motion begins to deviate from constant acceleration as the second phase of motion is approached.

Deformation Stage: The second phase of motion, transition to a cylindrical cap, begins with the penetration of a tongue of liquid into the bottom surface of the bubble. This is well predicted by the model and begins at $T = 0.6$. The predicted streamlines for both a stationary and moving observer are shown at four times during the transition phase in figure 4. Figure 5 shows the penetration quantitatively by plotting the vertical diameter of the bubble versus time for the period over which experimental data were reported. Also shown on this figure is a curve determined from the potential flow model of Walters and Davidson.[8] The data in figures 3 and 5 only represent the initial stages of large deformation. Beyond T=1.4 the photographic data reported by the experimenters must be used. Figure 6 shows a comparison of the photographs to the model predictions. The photographs clearly show that, in the later stages of transition to a steady flow, the penetration of liquid from below forms a trailing skirt. In frames 6 and 7 the experimental data shows some necking of this trailing skirt. This necking is quite important because it eventually becomes complete and results in a cylindrical cap with two small bubbles in its wake. This shedding is the mechanism by which vorticity is generated in the flow as it transforms from potential flow around a cylinder to fully separated flow behind a cylindrical cap.

The model results do not show such distinct shedding. Very small bubbles are shed from the trailing edge of the skirt but not from a clear necking process. However, the formation of a cylindrical cap with several small bubbles in the wake is very clear in frame 8. Other experiments using the same bubble injection technique[15] reported no trailing bubbles in the wake. However, they only reported

data after the cylindrical caps had reached terminal velocity. Since the wake is quite turbulent for an air/water bubble of this size (R = 26,700), the shed bubbles likely recirculate until they coalesce with the cap through its wavy floor and therefore do not consistently appear in the fully developed wake. Model development has not been pursued to the point where it is reasonable to expect turbulent flow in the wake to be accurately predicted since the model has no capacity to model turbulence at this time.

Cylindrical Approximation: Recall that the "cylindrical" bubbles in the experiments were contained between two plates 9.5mm apart whereas the model is truly two dimensional. A discussion of wall effects is given in Collins[30] but only as they pertain to the terminal velocity. It was concluded that two dimensional models underpredict the rise velocity of cylindrical bubbles created between parallel plates. Instability makes it impossible to create truly cylindrical bubbles in the laboratory. It is likely that the "laboratory" cylindrical bubble has a more stable skirt than the truly two dimensional bubble owing to the extra curvature present in the third dimension. It is not clear whether the differences in the shedding process are a result of deficiencies in the model or wall effects in the experiments.

Surface Tension: The specification of surface tension in the surface boundary condition is very important to the success of this model. The effects of attempting a prediction without the surface tension model can be seen in figure 7. The first difference was observed at the 75 ms point where a small bump began to grow on the top surface of the bubble. This bump continues to grow in the form of a disturbance propagating down the sides of the bubble. This behaviour is very different from the experimental results where the upper surface remains cylindrical. Implementing the surface tension model eliminated the initial formation of this disturbance allowing the upper surface to remain cylindrical. Even though surface tension is a relatively small force when the bubble size is large, it is vital to successful solutions since very small disturbances can otherwise grow unchecked and dominate the features of the bubble.

Grid Independence: To investigate the grid independence of the current solution a much finer grid was developed for the case of the rising cylindrical bubble. A 153 by 408 uniform grid yielding a

grid resolution of $\delta x = \delta y = 0.836mm$ and an equation set of order 62,424 was run for the first 40 ms ($T = 0.79$) of the simulation and showed no appreciable difference in the results up to that point.

Spherical Bubbles

Walters and Davidson[9] describe a similar study of initially spherical bubbles. Spherical bubbles ranging in volume from 110ml to 3000ml were released into a 45.7cm square by 0.91m high tank. The desired initial condition of a spherical bubble released from rest into a quiescent fluid was attained by bursting inflated balloons of various volumes with a remotely actuated needle while they were submerged in an otherwise liquid filled container. Upon bursting, the rigidity of the container maintained the constant volume of the bubble.

Initial Stage: As with the two dimensional work, the experimenters reported vertical displacement of the bubble versus time (see figure 8). Again the model results match the experimental data very well. Note that the initial acceleration of a spherical bubble released from rest is $2g$.

Deformation Stage: The penetrating liquid tongue is much harder to see in the photographs[9] because it is obscured by the resulting skirt. This made a direct comparison of the bubble silhouettes difficult in this case so the model results alone are presented in figure 9 for initial bubble volumes of 110 ml and 3000 ml. The beginning of the large deformation stage is again best characterised by plotting the vertical diameter versus time as in figure 10. The breakup resulting from penetration was into a very small spherical cap (often zero volume) and a rather large toroidal bubble.[9] This contrasts with the cylindrical case where the cap inherited the bulk of the initial volume. Because of this, no modelling of spherical cap bubbles was done. This would require a different set of initial conditions. Experimental studies of spherical caps usually use a dump cup mechanism.[10]

Toroidal bubble formation

The second part of Walters and Davidson[9] is concerned with the formation of a toroidal bubble. Air was injected into a tank to form toroidal bubbles of various volumes. After the bubble formed, by penetration of a tongue of liquid from below, they measured the circulation associated with the bubble by assuming it to be the core of a ring vortex. They found this circulation to be essentially constant as

the bubble rose with its ring diameter increasing and toroid diameter decreasing. Using the numerical technique described in this paper, spherical bubbles of various volumes (comparable to those in the experiments) were released and allowed to form into toroids. The circulation around these bubbles is easily computed from the velocity field and was found to be essentially constant after the toroid was formed. The Walters and Davidson[9] data for circulation versus the square root of the bubble volume are shown in figure 11 along with the model results.

CONCLUSIONS

The present finite difference model has been shown to effectively predict the initial motion of large gas bubbles released from rest in quiescent fluids. The impact of having a free surface in the interior of the solution domain has been considered in formulating convergence criteria and selecting iterative equation solvers. Further work is required to model the turbulent wake behind rising gas bubbles, which occurs later in their existence, and allow physically realistic breakup and coalescence to occur.

ACKNOWLEDGEMENTS

This project has been supported by a contract from the Environmental Emergencies Technology Division of Environment Canada and an operating grant from the Canadian Natural Sciences and Engineering Research Council. JDB is grateful for the award of a Killam Memorial Scholarship.

NOMENCLATURE

A	coefficient matrix
a	radius of curvature of bubble's leading edge
b	constant vector
C	portion of A
D	divergence in control volume
E	Eotvos number ($4ga_o^2\rho/\sigma$)
F	volume fraction of fluid
g	acceleration due to gravity
G	sub-matrix of A
H	sub-matrix Of A
I	identity matrix
K	tridiagonal portion of A
nx	number of control volumes in x direction

ny	number of control volumes in y direction
N	order of linear equation set
P	pressure
R	Reynolds number
s	stress
t	time
T	dimensionless time ($t\sqrt{g/a_o}$)
u	velocity in x direction
U	dimensionless velocity
v	velocity in y direction

Greek Symbols

α	void fraction
ΔP	pressure correction
δx	grid spacing in x direction
δy	grid spacing in y direction
ε	convergence criteria
Γ	circulation
κ	curvature
μ	dynamic viscosity
η	interpolation factor
ρ	liquid density
σ	surface tension
ω	relaxation factor

Subscripts

b	black
o	time zero
ij	control volume index
L	lower
pq	control volume index
r	red
s	at surface
U	upper

Superscripts

g	guess
m	iteration number
$m+1/2$	unrelaxed
n	time step number

REFERENCES

1. J.F. Harper, "The Motion of Bubbles and Drops Through Liquids", *Advances in Applied Mechanics* **12**, 59-129, (1972).
2. Lord Rayleigh, "On the Pressure Developed in a Liquid During the Collapse of a Spherical Cavity", *Philisophical Magazine, Series 6* **34**, 200,(1917).
3. S.A.Wilkerson, "Boundary Integral Techniques for Explosion Bubble Collapse", Energy Sources Technology Conference and Exhibition, Houston, January 22-25 , (1989).
4. R. Clift, J.R. Grace, and M.E. Weber, "Stability of Bubbles in Fluidized Beds", *Industrial and Chemical Engineering Fundamentals* **13**, 45-51, (1974).
5. W.J.Marble, T.L.Wong, F.J.Moody, and D.A.Hankins, "Retention of Fission Products by BWR Suppression Pools During Severe Reactor Accidents", International Thermal Nuclear Reactor

Safety Conference, Chicago, (1982).

6. C.L. Chen and V.K. Dhir, "Hydrodynamics of a Bubble Formed at Vent Pipe Exit", *International Journal of Multiphase Flow* **8**, 2, 147-163, (1982).
7. D.R. Topham, "Hydrodynamics of an Oilwell Blowout", Beaufort Sea Technical Report #33, (1975).
8. J.K.Walters and J.F.Davidson, "The Initial Motion of a Gas Bubble Formed in an Inviscid Liquid, Pt.1: The Two-dimensional Bubble", *Journal of Fluid Mechanics* **12**, 2, 408-417, (1962).
9. J.K.Walters and J.F.Davidson, "The Initial Motion of a Gas Bubble Formed in an Inviscid Liquid, Pt.2: The Three-dimensional Bubble and the Toroidal Bubble", *Journal of Fluid Mechanics* **17**, 3, 321-339, (1963).
10. R.M. Davies and G.I. Taylor, "The Mechanics of Large Bubbles Rising Through Extended Liquids and Through Liquids in Tubes", *Proceedings of the Royal Society. Series A* 200, 375-390, (1950).
11. J.T.Lindt, "Note on the Wake Behind a Two-dimensional Bubble", *Chemical Engineering Science* **26**, 1776-1777, (1971).
12. J.T.Lindt, "On the Periodic Nature of the Drag on a Rising Bubble", *Chemical Engineering Science* **27**, 1775-1781, (1972).
13. J.R.Crabtree and J.Bridgewater, "The Wakes Behind Two-dimensional Air Bubbles", *Chemical Engineering Science* **22**, 1317-1518, (1967).
14. R.Collins, "Structure and Behaviour of Wakes behind Two-dimensional Air Bubbles in Water", *Chemical Engineering Science* **20**, 851-85, (1965).
15. W.F.Bessler and H.Littman, "Experimental Studies of Wakes behind Circularly Capped Bubbles", *Journal of Fluid Mechanics* **185**, 137-151, (1987).
16. P.P. Wegener and J. Parlange, "Spherical-Cap Bubbles", *Annual Review of Fluid Mechanics* **5**, 79-100, (1973).
17. L.Rosenhead, "The Formation of Vortices from a Surface of Discontinuity", *Proceedings of the Royal Society. Series A* **134**, 170-192, (1931).
18. G.Tryggvason and H.Aref, "Numerical Experiments on Hele Shaw Flow with a Sharp Interface", *Journal of Fluid Mechanics* **136**, 1-30, (1983).
19. S.H.Brecht and J.R.Ferrante, "Vortex-in-cell Simulations of Buoyant Bubbles in Three Dimensions", *Physics of Fluids* **7**, 1166-1191, (1989).
20. J.C.S.Meng and J.A.L.Thomson, "Numerical Studies of some Nonlinear Hydrodynamic Problems by Discrete Vortex Element Methods", *Journal of Fluid Mechanics* **84**, 433-453, (1978).
21. G.Ryskin and L.G.Leal, "Numerical Solution of Free Boundary Problems in Fluid Mechanics. Part 1. The Finite-difference Technique", *Journal of Fluid Mechanics* **148**, 1-17, (1984).
22. G.Ryskin and L.G.Leal, "Numerical Solution of Free Boundary Problems in Fluid Mechanics. Part 2. Buoyancy Driven Motion of a Gas Bubble Through a Quiescent Liquid", *Journal of Fluid Mechanics* **148**, 19-35, (1984).
23. B.D.Nichols, C.W.Hirt, and R.S.Hotchkiss, "SOLA-VOF: A Solution Algorithm for Transient Fluid Flow with Multiple Free Boundaries", LA-8355, (1980).
24. F.H.Harlow and J.E.Welch, "Numerical Calculation of Time-Dependent Viscous Incompressible Flow of Fluid with Free Surface", *Physics of Fluids* **8**, 2182-2189, (1965).
25. R.D.Rowe and J.D.Bugg, "A Numerical Study of Large Bubble Dynamics", Canadian Applied Mathematics Society of Continuum Mechanics and its Applications, Hemisphere Publishing Corp., Vancouver, 611-620 , (June 2, 1988).
26. B.D.Nichols and C.W.Hirt, "Numerical Simulation of Boiling Water Reactor Vent-Clearing Hydrodynamics", *Nuclear Science and Engineering* **73**, 196-209, (1980).

27. L.A.Hageman and D.M.Young, *Applied Iterative Methods*, Academic Press, New York, (1981).

28. S.V.Patankar, *Numerical Heat Transfer and Fluid Flow*, Hemisphere, New York, (1980).

29. Control Data Corporation(CDC), *MAGEV: Mathematical and Geophysical Vector Library, Version 3.3* , (1984).

30. R.Collins, "A Simple Model of the Plane Gas Bubble in a Finite Liquid", *Journal of Fluid Mechanics* 22, 763-771, (1965).

LIST OF FIGURES

Figure 1: Surface pressure interpolation technique ($\eta_{ij} = d/b$).

Figure 2: Ordering scheme: (a)Natural, (b)Red-black point and (c)Red-black line.

Figure 3: Position versus time for a cylindrical bubble released from rest into a quiescent liquid. Experimental data of Walters and Davidson[8].

Figure 4: Stream function contours for the initial motion of a cylindrical bubble released from rest in a quiescent liquid (Uniform contour intervals). Right side: stationary observer. Left side: Observer on bubble.

Figure 5: Vertical diameter versus time for a cylindrical bubble released from rest into a quiescent liquid. Experimental data of Walters and Davidson[8].

Figure 6: Cylindrical bubble predictions compared to photographs of Walters and Davidson[8].

Figure 7: Effect of neglecting surface tension on cylindrical bubble predictions.

Figure 8: Position versus time for a spherical bubble released from rest into a quiescent fluid. Experimental data of Walters and Davidson[9].

Figure 9: Prediction of initial motion of spherical bubbles released from rest into a quiescent liquid. (a) 3000 *ml* bubble (b) 110 *ml* bubble (shown double size).

Figure 10: Vertical diameter versus time for a spherical bubble released from rest into a quiescent liquid. Experimental data of Walters and Davidson[9].

Figure 11: Circulation associated with toroidal bubble versus bubble volume. Experimental data of Walters and Davidson[9].

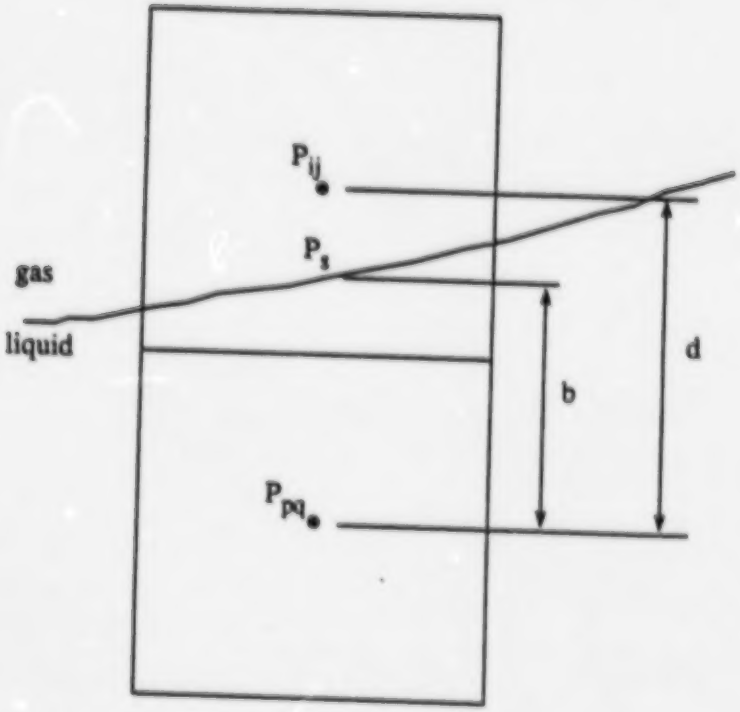

Figure 1

36	37	38	39	40	41	42
29	30	31	32	33	34	35
22	23	24	25	26	27	28
15	16	17	18	19	20	21
8	9	10	11	12	13	14
1	2	3	4	5	6	7

(a)

39	19	40	20	41	21	42
15	36	16	37	17	38	18
32	12	33	13	34	14	35
8	29	9	30	10	31	11
25	5	26	6	27	7	28
1	22	2	23	3	24	4

(b)

36	37	38	39	40	41	4
15	16	17	18	19	20	2
29	30	31	32	33	34	3
8	9	10	11	12	13	1
22	23	24	25	26	27	2
1	2	3	4	5	6	7

(c)

Figure 2

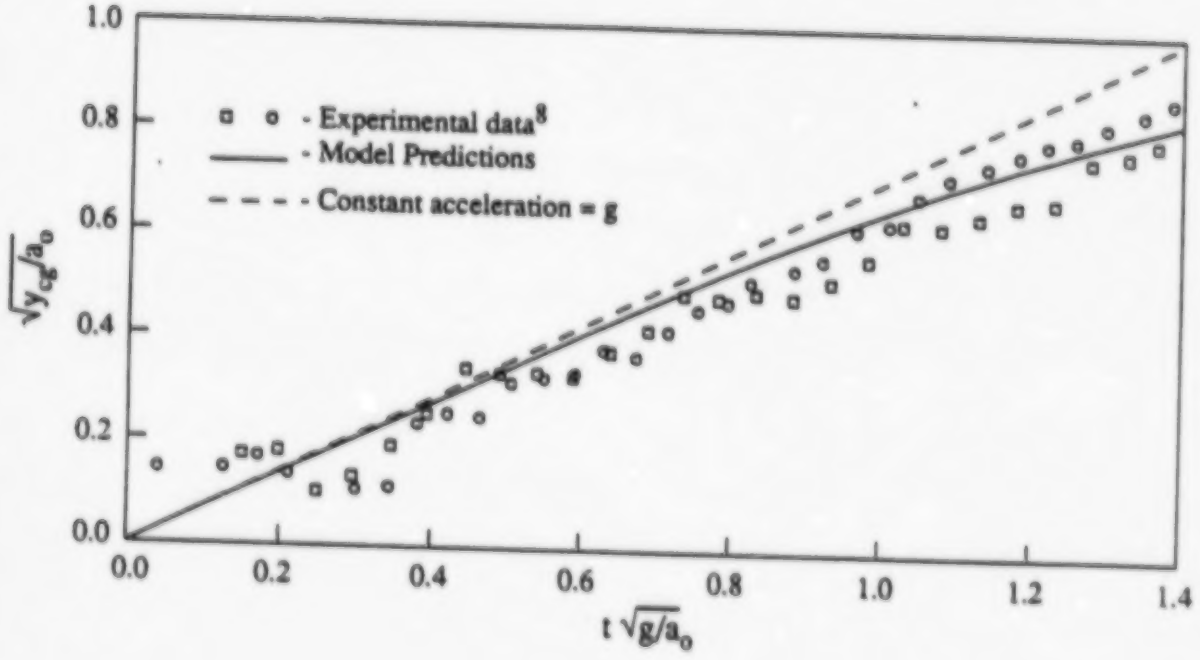
1.0
0.8
0.6
0.4
0.2
0.0
0.0
0.2
0.4
0.6
0.8
1.0
1.2
1.4
□ ○ - Experimental data[8]
— - Model Predictions
- - - - Constant acceleration = g
$\sqrt{y_{cg}/a_o}$
$t\sqrt{g/a_o}$

Figure 3

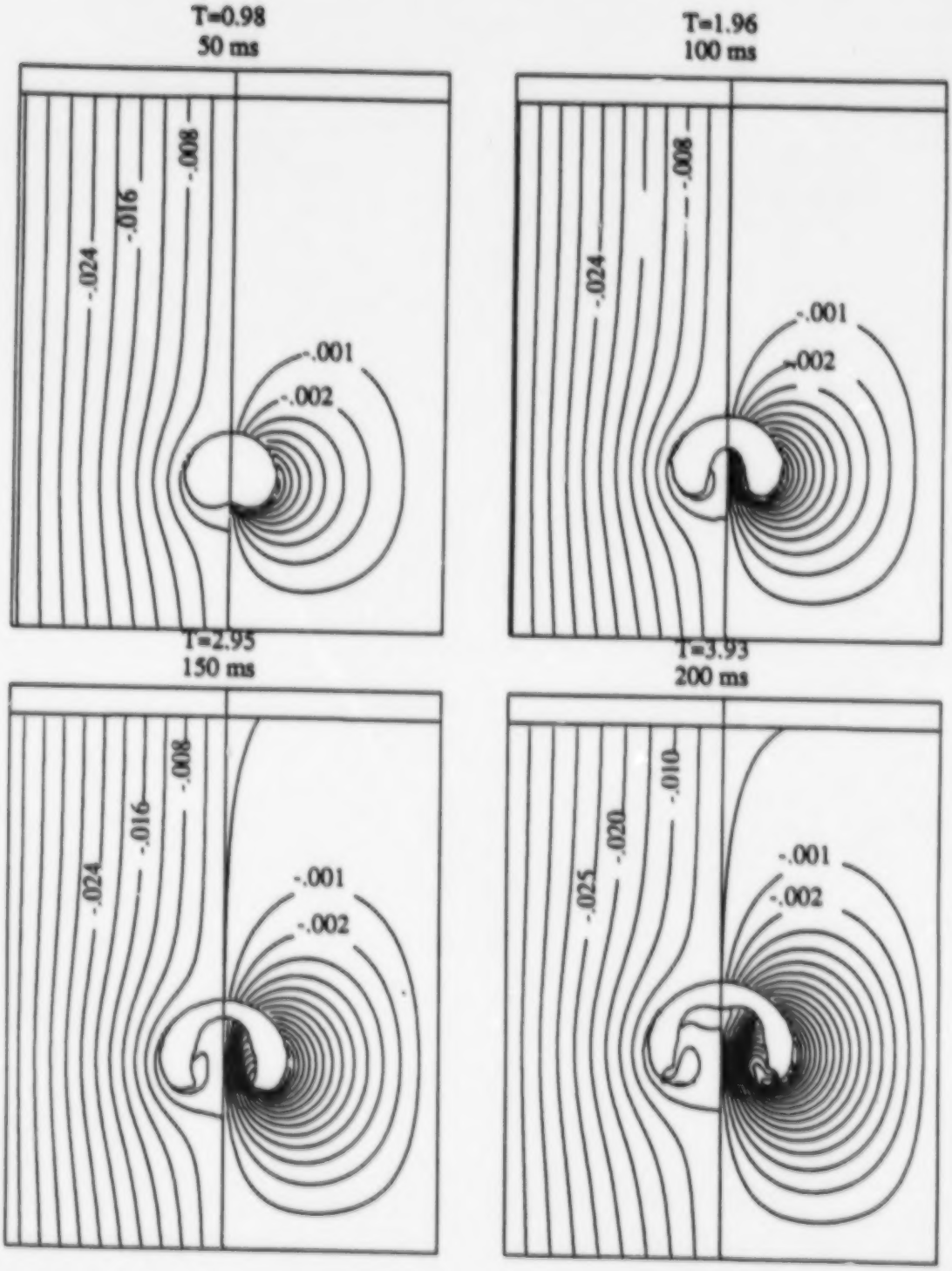
T=0.98
50 ms
-.024
-.016
-.008
-.001
-.002
T=1.96
100 ms
-.024
-.008
-.001
-.002
T=2.95
150 ms
-.024
-.016
-.008
-.001
-.002
T=3.93
200 ms
-.025
-.020
-.010
-.001
-.002

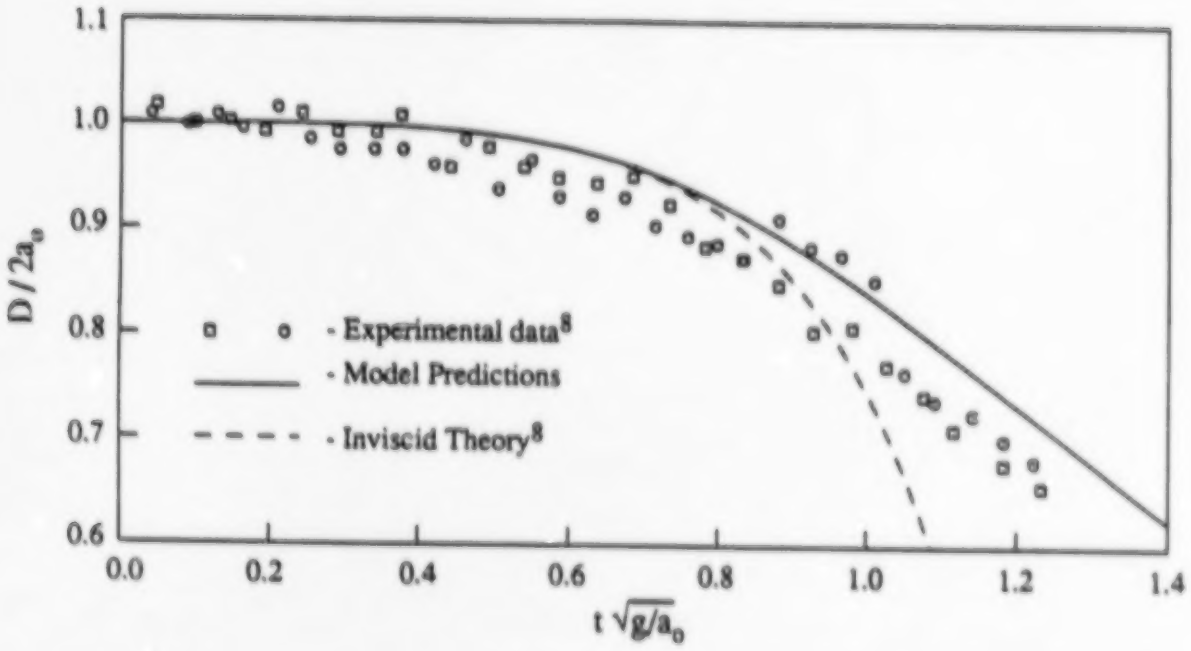
1.1
1.0
0.9
0.8
0.7
0.6
D / 2a$_o$
- Experimental data[8]
- Model Predictions
- Inviscid Theory[8]
0.0
0.2
0.4
0.6
0.8
1.0
1.2
1.4
t $\sqrt{g/a_o}$

Figure 5

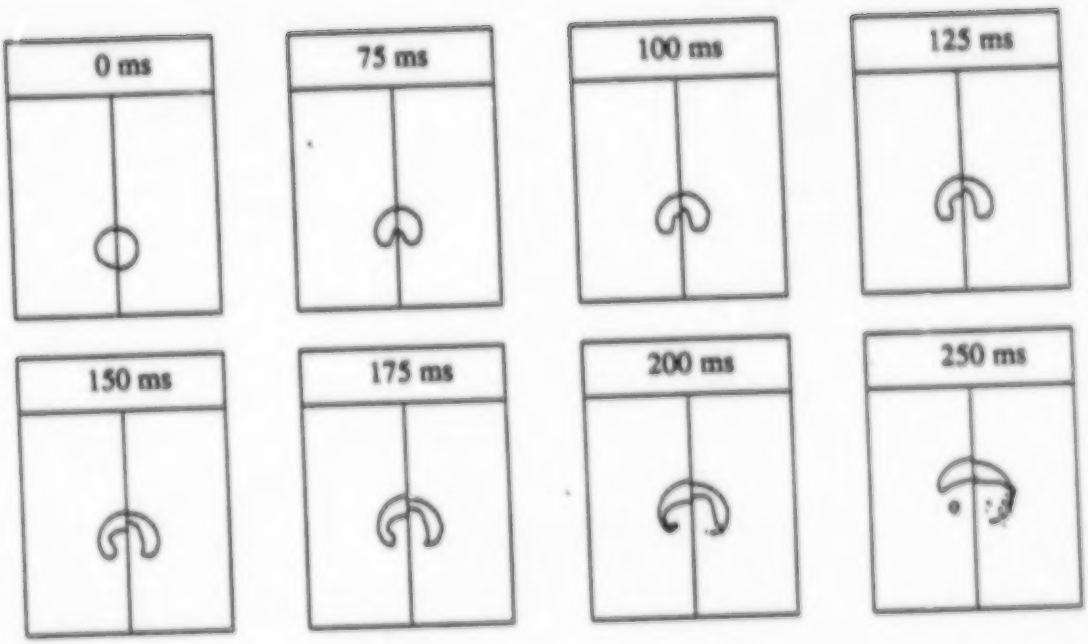

Figure 6

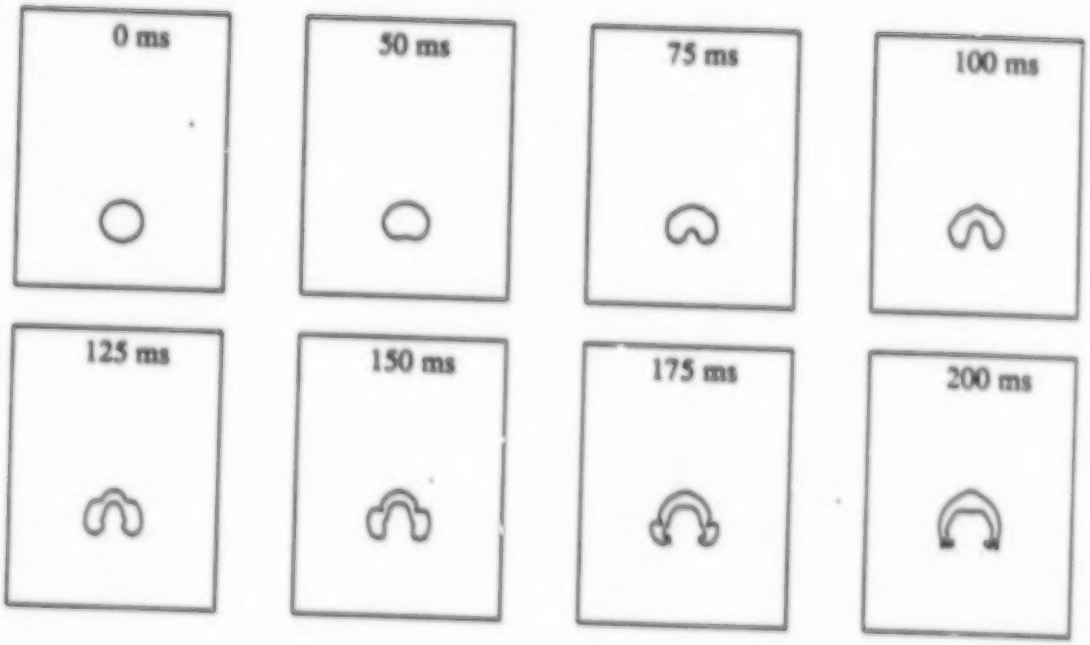

Figure 7

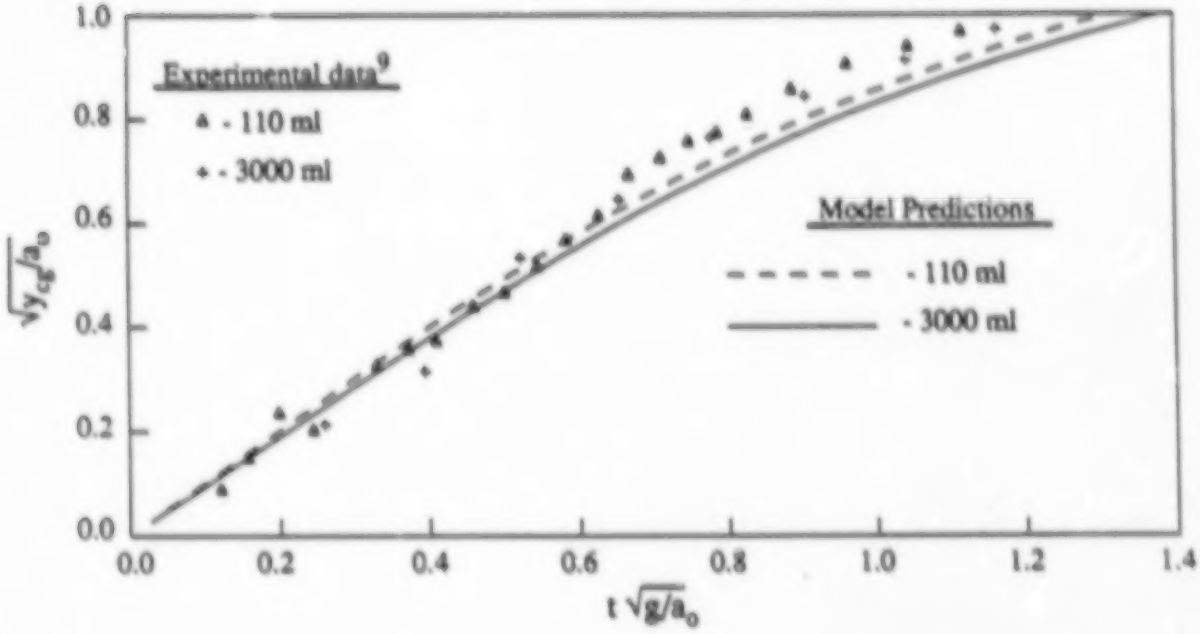
Experimental data[9]
▲ - 110 ml
◆ - 3000 ml
Model Predictions
- 110 ml
- 3000 ml
$\sqrt{y_{cg}/a_o}$
$t\sqrt{g/a_o}$
0.0
0.2
0.4
0.6
0.8
1.0
1.2
1.4

Figure 8

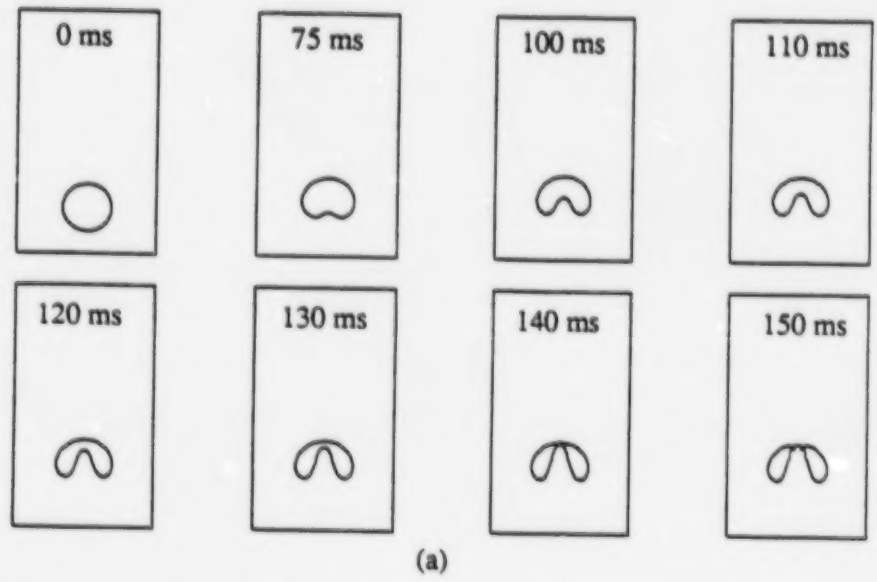
0 ms
75 ms
100 ms
110 ms
120 ms
130 ms
140 ms
150 ms

(a)

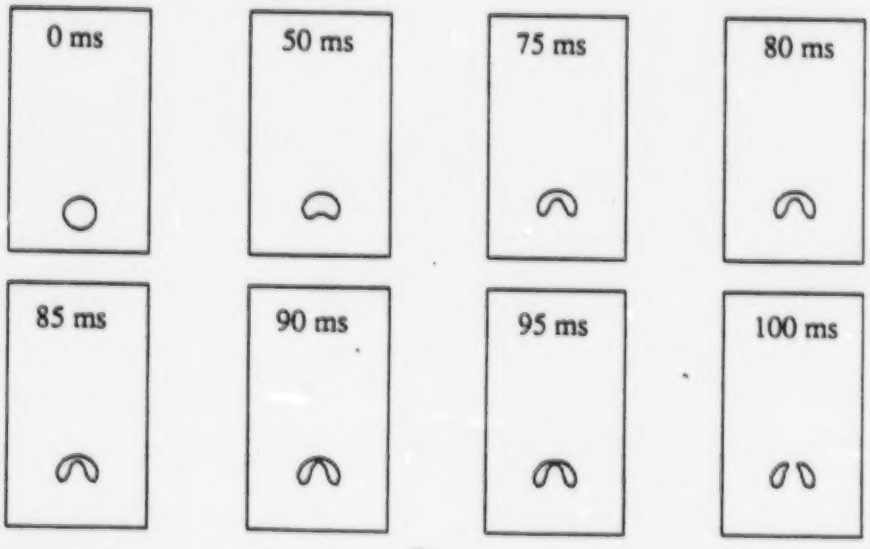
0 ms
50 ms
75 ms
80 ms
85 ms
90 ms
95 ms
100 ms

(b)

Figure 9

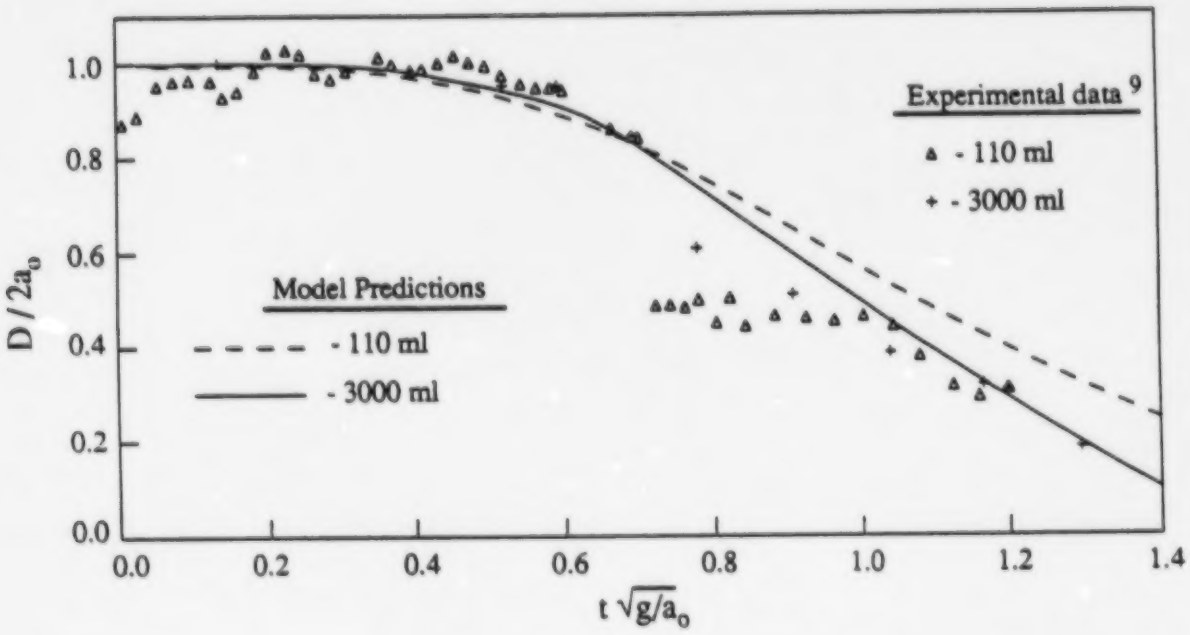
Experimental data [9]
- 110 ml
- 3000 ml
Model Predictions
- 110 ml
- 3000 ml
D / 2a_o
t √(g/a_o)
0.0
0.2
0.4
0.6
0.8
1.0
1.2
1.4

Figure 10

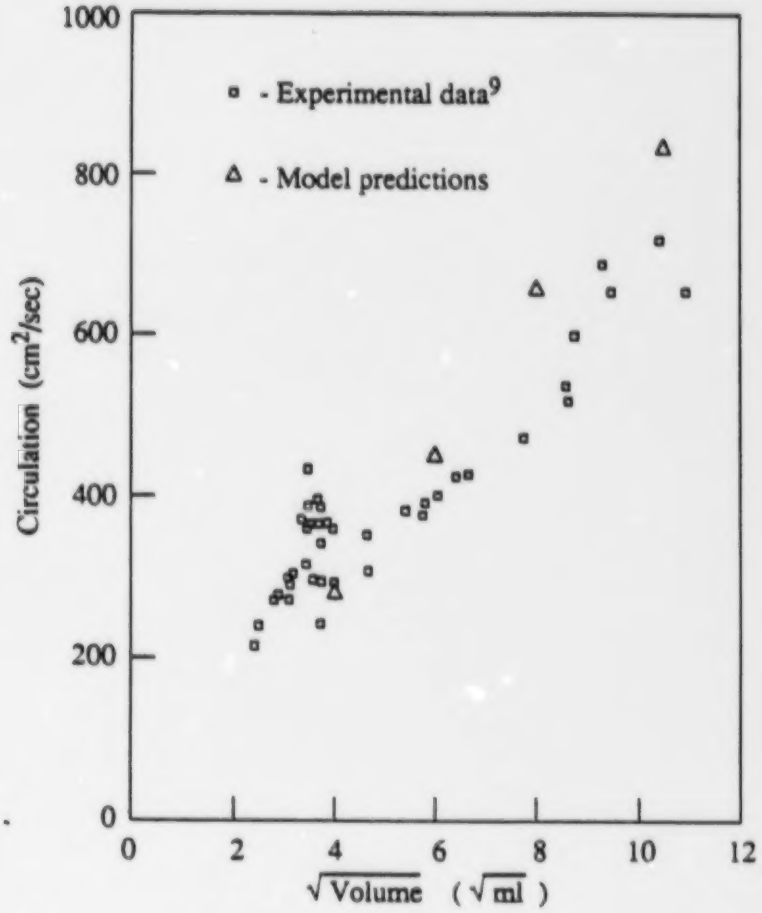
1000
800
600
400
200
0
0
2
4
6
8
10
12
□ - Experimental data[9]
△ - Model predictions
Circulation (cm²/sec)
√Volume (√ml)

Figure 11